

Unveiling BLR Structure in AGN with High Resolution X-ray Spectra

An Analytic Approach to Wind Emission Line Profiles

Scott Hagen^{1,2,3,4}, Chris Done⁴, Gabriele A. Matzeu⁵, and Hirofumi Noda⁶

¹ IFPU - Institute for Fundamental Physics of the Universe, Via Beirut 2, 34151 Trieste, Italy
e-mail: shagen@sissa.it

² SISSA - International School for Advanced Studies, Via Bonomea 265, 34136 Trieste, Italy

³ INAF - Osservatorio Astronomico di Trieste, Via G. B. Tiepolo 11, I-34143 Trieste, Italy

⁴ Centre for Extragalactic Astronomy, Department of Physics, Durham University, South Road, Durham DH1 3LE, UK

⁵ Quasar Science Resources SL for ESA, European Space Astronomy Centre (ESAC), Science Operations Department, 28692, Villanueva de la Cañada, Madrid, Spain

⁶ Astronomical Institute, Tohoku University, 6-3 Aramakiazaaoba, Aoba-ku, Sendai, Miyagi 980-8578, Japan

Received September 30, 20XX

ABSTRACT

XRISM has provided an unprecedented view of the emission and absorption lines in the X-ray. Notably, early results showed significant complexity to the Fe- $K\alpha$ line profile in AGN, with clear contributions from at least three emitting structures: an inner disc, intermediary broad line region (BLR) scale material, and an outer torus. This poses a new challenge for the modelling of the emission lines, as while fast sophisticated models exist for disc line-profiles, large scale-height material is typically much more complex. In this paper we aim to address this gap, by building a fully analytic model for the emission line profiles from a wind, aimed towards BLR scale material, motivated on previous reverberation studies suggesting a wind on the inner edge of the BLR. Our approach give a physically motivated, yet computationally fast, model for the intermediary component to the Fe- $K\alpha$ complex seen in the XRISM data. We demonstrate our model on the XRISM observations of NGC 4151 from the performance verification phase, showing that it gives a good description of the data, with physically reasonable parameters for BLR scale material. We also show that our model naturally gives the ‘smooth’ line profile seen in the data, due to the large spatial extent of a wind. Finally, we make our model code public to the community, and name it xwind.

Key words. Accretion, accretion disks – Line: profiles – X-rays: galaxies

1. Introduction

Accreting systems, typically understood in the context of the [Shakura & Sunyaev \(1973\)](#) disc model, display near ubiquitous out-flowing winds. From accreting white-dwarves, to black hole binaries, and up to active galactic nuclei, outflowing material seems to be a direct consequence of accretion; either driven via magnetic fields (e.g. [Blandford & Payne 1982](#); [Fukumura et al. 2010, 2017](#)), thermally through inverse Compton scattering (e.g. [Begelman et al. 1983](#); [Begelman & McKee 1983](#)), or radiatively via the absorption of an incident photon field (e.g. [Proga et al. 2000](#); [Proga & Kallman 2004](#); [King 2010](#)).

In AGN the picture is rather complex. In the X-ray there are the ultra-fast outflows (UFOs), winds reaching a significant fraction of the speed of light ($\sim 0.2 - 0.3c$) typically associated with highly accreting AGN (e.g. [Reeves et al. 2009](#); [Tombesi et al. 2010](#); [Nardini et al. 2015](#); [Matzeu et al. 2017](#); [Igo et al. 2020](#); [Xrism Collaboration et al. 2025](#); [Noda et al. 2025b](#)). In the optical/UV powerful outflows can manifest in both characteristic broad-absorption lines (e.g. [Weymann et al. 1991](#); [Leighly et al. 2009, 2018](#); [Choi et al. 2020, 2022](#)) or skewed and blue-shifted emission lines. Importantly for our understanding of AGN feedback, these powerful outflows are detected across cosmic time (e.g. [Maiolino et al. 2012](#); [Bischetti et al. 2017, 2019, 2023](#); [Fiore et al. 2017](#)), with a clear link between the outflow power

and the accretion power in the AGN (e.g. [Feruglio et al. 2015](#); [Fiore et al. 2017](#)).

However, the majority of AGN, especially in the local Universe, are not accreting close to the Eddington limit, and so one does not necessarily expect to see these powerful outflows. Yet, even in more typical moderately accreting AGN, there is evidence for winds; albeit with significantly less power than the more extreme UFOs. The clearest examples coming from the intensive monitoring campaigns, in particular the STORM campaigns ([De Rosa et al. 2015](#)), which showed clear evidence of variable absorption, now interpreted as a disc wind on the inner edge of the BLR ([Dehghanian et al. 2019a,b](#); [Kara et al. 2021](#)). More recently, BLR scale outflows have also been suggested in spatially resolved Gravity/Gravity+ observations (e.g. [GRAVITY Collaboration et al. 2024](#); [GRAVITY+ Collaboration et al. 2025](#)). Given the prevalence of more moderately accreting AGN and the near ubiquitous presence of the BLR, understanding the structure of these BLR scale outflows and their link to the accretion flow is critical for our overall understanding of AGN structure and evolution.

Large scale-height material has the advantage that it subtends a large solid angle as seen from the central source. Given the ubiquity of high energy X-rays in AGN ([Elvis et al. 1994](#); [Lusso & Risaliti 2016](#)), this large scale height material should see, and absorb, a significant number of X-ray photons. A fraction of these will then be re-emitted, predominantly in Fe-

$\text{K}\alpha$ and $\text{Fe-K}\beta$ (e.g. Murphy & Yaqoob 2009; Tzanavaris et al. 2023), with the motion of the material imprinted onto the observed line shape. Indeed prior work using Chandra, XMM, and NuSTAR spectra have shown clearly contributions to the $\text{Fe-K}\alpha$ line from BLR scale material (e.g. Yaqoob & Padmanabhan 2004; Bianchi et al. 2008; Miller et al. 2018; Andonie et al. 2022b,a). This is further supported by Noda et al. (2023) who showed the $\text{Fe-K}\alpha$ lagging the continuum through a changing-state event with time-scales corresponding to BLR distances.

More recently, XRISM observations of bright, nearby, AGN have clearly distinguished multiple components to the $\text{Fe-K}\alpha$ complex, consistently showing an intermediary component consistent with BLR scale material (Xrism Collaboration et al. 2024; Bogensberger et al. 2025; Miller et al. 2025; Mehdipour et al. 2025; Kammoun et al. 2025). This provides an opportunity, as resolving individual components to the emission lines allows for the detailed modelling of each of these emitting components. However, herein lies the challenge, as detailed modelling of wind emission lines is generally complex. Firstly, physically realistic modelling of the wind structures requires expensive hydrodynamical simulations (e.g. Proga et al. 2000; Nomura et al. 2016; Nomura & Ohsuga 2017; Higginbottom et al. 2018). This can be circumvented to some extent by implementing parametric models for the wind structure (e.g. Knigge et al. 1995; Sim et al. 2008; Hagino et al. 2015; Matzeu et al. 2022; Luminari et al. 2018, 2024), which allow for rapid calculations of both the velocity and density profiles. This approach is used in a number of current AGN wind models (e.g. the WINE model of Luminari et al. 2024 and the xRADE model from Matzeu et al. 2022, among others). However, in order to extract observable spectra, radiative transfer calculations are required, regardless of whether the wind structure is calculated via simulation or parametrically. Radiative transfer calculations are typically complex, leading to computational bottlenecks; although we note a number of sophisticated methods do currently exist (e.g. Long & Knigge 2002; Odaka et al. 2011; Mehdipour et al. 2016; Ferland et al. 2017; Vander Meulen et al. 2023; Luminari et al. 2023; Matthews et al. 2025). Often, to speed up the fitting process, studies will then resort to calculating model grids to create interpolation tables (e.g. Luminari et al. 2024), or for more advanced usage train a convolutional neural net (Matzeu et al. 2022) (emulation). These are highly advanced models, with the ability to fit a full broad-band X-ray spectrum. However, for a slow wind on the inner edge of the BLR, the main constraining power in the X-ray should originate in the $\text{Fe-K}\alpha$ complex, and so performing full radiative transfer is likely unnecessary.

Instead, it should be possible to perform a simplified analytic calculation. This is the main aim of this paper. Here we parametrise the wind in terms of its geometry, velocity profile, and mass-outflow rate. Through mass-conservation we then calculate the density profile. Under the assumption that the material is mostly neutral, and illuminated by a simple power-law X-ray spectrum, we perform a simplified calculation of the absorption and transmittance of the incident X-ray spectrum through the wind. This approach is analytic, and allows us to extract the number of photons re-emitted in $\text{Fe-K}\alpha$, in essence the emissivity profile. Accounting for the relativistic Doppler shift induced by the wind motion, and integrating over the emissivity profile, then gives the observed frame emission line profile. This not only provides a rapid calculation of the emission line profile, it also self-consistently calculates the equivalent width of the line. These combine to give constraining power on not only

the distance from the black hole of the wind, but also the mass-outflow rate and covering fraction.

This paper is organised as follows. In section 2 we define the model, and give a detailed description of the calculations. Then in section 3 we explore the properties of the model and its observables. In section 4 we apply our model to a XRISM observation of NGC4151, demonstrating its ability to constrain the properties of a BLR like wind, before we give our discussion and conclusions in section 5.

2. XWIND model definition

We give here a detailed overview of the calculations that go into our wind line model. Throughout we will use the standard notation for radii, where r is dimensionless gravitational radius and R is in physical units, related via $R = rR_G$ where $R_G = GM/c^2$. This same notation also applies to any other distance measure throughout this paper.

2.1. Wind Geometry

We start by defining the geometry of our wind, sketched in Fig. 1, expanding upon that initially defined in Sim et al. (2008). Throughout we will work in spherical polar coordinates. For simplicity we assume the wind is axisymmetric in azimuth, eliminating any dependence on ϕ in *the reference frame of the wind*.

As in Sim et al. (2008) the wind is launched between r_{in} and r_{out} . We consider the wind to consist of a set of streamlines, each with opening angle α_{ij} , which all converge at a focal point d_f located on the z-axis directly below the origin. We treat this focal point as an input parameter throughout our calculations. The maximum extent of the wind is then set by the covering fraction f_{cov} , defined in terms of the total solid angle $f_{\text{cov}} = \Omega/4\pi$. While this assumes the wind is launched from both sides of the disc, the observer will only see emission originating from the side of the disc facing the observer. This gives a spherical boundary condition of r_{max} defined as:

$$r_{\text{max}} = \frac{r_{\text{in}}}{\sin(\theta_{\text{min}}) - \frac{r_{\text{in}}}{d_f} \cos(\theta_{\text{min}})} \quad (1)$$

where $\cos(\theta_{\text{min}}) = f_{\text{cov}}$ (from the definition of the solid angle). We stress that this boundary condition is only valid if $\arccos(f_{\text{cov}}) > \arctan(r_{\text{in}}/d_f)$, as otherwise the opening angle of the wind is too shallow to ever reach the desired covering fraction. In these instances our model code will throw a warning, and then re-adjust f_{cov} , before proceeding with the calculation.

We now depart somewhat from the geometry in Sim et al. (2008), here opting to divide our wind into cells in θ and r . We define bins in $\cos(\theta)$, spaced at a constant $d\cos(\theta) = 0.002$, in the range $\cos(\theta) \in [0, f_{\text{cov}}]$. This naturally leads to each wind cell subtending the *same* solid angle $d\Omega = d\phi d\cos(\theta)$ as seen from the central source. When evaluating wind properties we use the centre of each bin, defined as $\theta_i = \cos(\theta_{\text{edge}}) + 0.5d\cos(\theta)$, where θ_{edge} is the lower edge of the bin.

For each θ_i , we then further subdivide in bins of r , geometrically spaced such that $d\log(r) = 0.01$ is constant. Here the radial bin edges are defined from the point where the sight-line along θ_i crosses the streamline launched from r_{in} to the point where the sight-line *either* crosses the streamline from r_{out} or where it crosses r_{max} ; whichever is smallest. As with θ , we evaluate the wind properties at the centre of the bin, defined as $r_j = r_{\text{edge}} + 0.5 \times 10^{\log_{10}(r_{\text{edge}}) + d\log(r)}$.

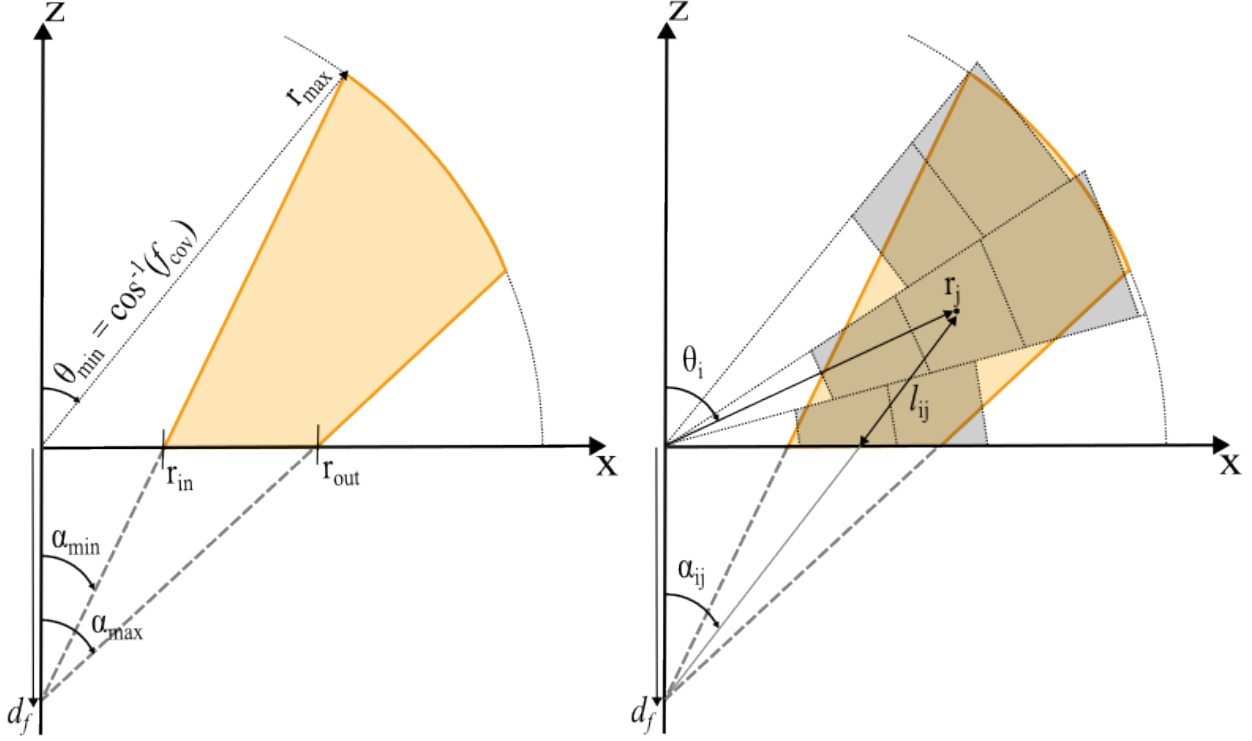


Fig. 1: **Left:** Definition of our model geometry. The wind is launched between r_{in} and r_{out} , at an angle defined by the distance of the focus below the origin, d_f . The covering fraction f_{cov} defines the maximum radial extent of the wind r_{max} (in spherical polar coordinates), giving a spherical boundary condition.

Right: Example of our calculation grid (at significantly lower resolution for clarity). We split the wind into cells of $\cos(\theta)$ with width $d \cos(\theta)$ in the range $\cos(\theta) \in [0, f_{\text{cov}}]$, and radius r with width $d \log(r)$. The grid in r extends from the inner streamline to either the outer streamline (defined from r_{out}) or r_{max} , depending on whichever is smallest. Our wind cells are illustrated as the dark shaded regions. Throughout this paper we will evaluate the wind emission and density at the centre of each cell θ_i and r_j . For completeness, this also defines the length travelled along the streamline l_{ij} at each cell.

The wind is now tiled by a set of cells, each with evaluation points θ_i and r_j . This is illustrated in the right side of Fig. 1. Each of these cells correspond to a streamline launched at $r_{L,ij}$ with opening angle α_{ij} , and evaluated at a length l_{ij} along the streamline. These are all given by:

$$\cos(\alpha_{ij}) = \frac{r_j \cos(\theta_i) + d_f}{[r_j^2 + 2r_j d_f \cos(\theta_i) + d_f^2]^{1/2}} \quad (2)$$

$$r_{L,ij} = d_f \tan(\alpha_{ij}) \quad (3)$$

$$l_{ij} = [r_j^2 + r_{L,ij}^2 - 2r_j r_{L,ij} \sin(\theta_i)]^{1/2} \quad (4)$$

2.2. Velocity Profile

The velocity profile can now be easily calculated for each wind cell. Starting with the azimuthal velocity v_ϕ , we assume that at the base of the wind the streamline has the same azimuthal velocity as the disc, taken here to be Keplerian. As material travels out along the streamline, angular momentum is conserved, such that the azimuthal velocity at any point in the wind is (Knigge et al. 1995):

$$\frac{v_\phi}{c} = \frac{r_L}{r} \sqrt{\frac{1}{r_L}} \quad (5)$$

Note that here we have dropped explicit reference to the cell indexes i and j .

The second component is the outflowing velocity along a streamline. Here we use the velocity profile parametrised in terms of the velocity at infinity v_∞ (Knigge et al. 1995; Sim et al. 2008; Hagino et al. 2015, 2016; Matzeu et al. 2022):

$$v_l = v_0 + (v_\infty - v_0) \left(1 - \frac{r_v}{r_v + l}\right)^\beta \quad (6)$$

Here v_0 is the initial velocity at the base, which we fix to 0 throughout. r_v is the velocity scale length, defined as the distance along the streamline where the velocity reaches half of v_∞ , and β is the velocity exponent that determines the rate of acceleration along a streamline. l is the distance along the streamline, previously given in Eqn. 4.

2.3. Density Profile

Given the defined geometry and corresponding velocity profile, we can now estimate the density profile of the wind, following Matzeu et al. (2022). We start by considering a total mass-outflow rate \dot{M}_w . It is often easier to express this in terms of the

Eddington mass-accretion rate, \dot{M}_{Edd} , as this naturally scales by the mass of the central object, such that $\dot{m}_w = \dot{M}_w / \dot{M}_{\text{Edd}}$.

The mass outflow is distributed between r_{in} and r_{out} , with a mass-loss rate per unit area given by $d\dot{M}_w/dA \propto R_L^\kappa$. Here κ determines the efficiency of the wind as a function of physical launch radius. For radiatively driven outflows the expectation is that $\kappa \sim -1.3 \rightarrow -1$ (Behar 2009), which effectively states that the majority of the material is launched from the inner edge of the wind, with the outflow becoming increasingly inefficient as the launch radius increases.

Mass conservation requires that:

$$\dot{M}_w = 2 \int_S \frac{d\dot{M}_w}{dA} dA = 2 \int_0^{2\pi} d\phi \int_{R_{\text{in}}}^{R_{\text{out}}} \frac{d\dot{M}_w}{dA} R dR \quad (7)$$

This is simply the integral across the surface of the disc covered by the wind (i.e the annulus between r_{in} and r_{out}), and the factor of 2 comes from the disc having two sides. This can be solved analytically, to give:

$$\begin{aligned} \frac{d\dot{M}_w}{dA} &= \frac{\dot{M}_w(\kappa + 2)}{4\pi[R_{\text{out}}^{\kappa+2} - R_{\text{in}}^{\kappa+2}]} R_L^\kappa \\ &= \frac{\dot{m}_w \dot{M}_{\text{Edd}}(\kappa + 2)}{4\pi[r_{\text{out}}^{\kappa+2} - r_{\text{in}}^{\kappa+2}]} r_L^\kappa R_G^{-2} \end{aligned} \quad (8)$$

For a given wind cell, we can write the mass density as $\rho = dM/dV$, where $dV = dAdz$. Further, within a cell the material has a velocity along the streamline v_l , such that in time dt it has travelled $dz = v_l dt$. Hence we can write $dV = v_l dt dA$, such that $\rho = d\dot{M}_w / (v_l dA)$. The number density in a wind cell is then given by:

$$n = \frac{\rho}{m_I} = \frac{1}{m_I v_l} \frac{d\dot{M}_w}{dA} \quad (9)$$

where $m_I \simeq 1.23m_p$ is the ion mas, which we choose to write in terms of the proton mass m_p . the left column of Fig. 2 demonstrates the density profile for a wind launched at BLR like distances over a range of outflow velocities.

2.4. Calculating the emissivity

An important aspect in the shape of the emission line is the relative emissivity across the wind volume. For a photo-ionised line this can be calculated from an incident spectrum and wind density profile. We give here an overview of our methodology for this, based on the neutral Fe-K α line. We stress, that the below calculations give self-consistent solutions to the Fe-K α line strength, however for other emission lines this is not the case. Hence within xwind, we provide two submodels: xwindline, where the normalisation should remain free for generic use, and xwindfe, where the normalisation is self-consistently calculated for neutral Fe-K α and the rest-frame emission assumes the 7-Lorentzian approximation from Hölzer et al. (1997). Internally, the calculations are identical, as xwindline uses the emissivity calculated assuming neutral Fe-K α . We also use xwindline to extract a convolution kernel, xwindconv, allowing for the application of wind broadening to any spectral-shape, including continuum. Throughout we neglect the Compton shoulder in xwind, as the typical wind densities are too low for this to be important; with the exception perhaps at the base of the wind.

We base our calculations on the analytic approach given in Yaqoob et al. (2001), updated in Tzanavaris et al. (2023). Firstly, the wind will see an incident spectrum, $N(E)$, originating from the central regions of the accretion flow. The relevant part of the spectrum depends somewhat on the line species being calculated, due to strongly differing ionisation potentials. However, this is too complex for our approach. Instead we assume that the *relative* emissivity across the wind volume is more or less identical for each line species (i.e that for all lines it traces density), and only the absolute (i.e normalisation) emissivity differs. Thus, internally we calculate the absolute emissivity for neutral Fe-K α , and simply apply the same emissivity for any other line.

The neutral Fe-K α line is induced by photons above $E_K \simeq 7.1 \text{ keV}$. In this energy range the intrinsic emission is dominated by inverse Compton scattering, giving a power-law like spectrum (Haardt & Maraschi 1993; Haardt et al. 1994). Hence, we fix the incident spectrum to a power-law of the form $N(E) = N_0 E^{-\Gamma}$, photons $\text{s}^{-1} \text{ cm}^{-2} \text{ keV}^{-1}$. In xwindfe N_0 is the number of photons $\text{s}^{-1} \text{ cm}^{-2}$ at 1 keV. Following Tzanavaris et al. (2023), the emitted Fe-K α photon flux from a constant column-density material with a solid angle Ω is:

$$N_{\text{Fe-K}\alpha} = \frac{\Omega}{4\pi} y \int_{E_K}^{\infty} N(E) \{1 - \exp(-\sigma_{\text{Fe-K}}(E) A_{\text{Fe}} N_H)\} dE \quad (10)$$

where $y \sim 0.3$ is the fluorescent yield, $A_{\text{Fe}} \simeq 4.86 \times 10^{-5}$ (Anders & Grevesse 1989) is the iron abundance, N_H is the column-density of the absorbing material, and $\sigma_{\text{Fe-K}}$ is the iron K-shell absorption cross-section. The cross-section decays exponentially with energy above the absorption edge, such that $\sigma_{\text{Fe-K}}(E) = \sigma_0(E/E_K)^{-\alpha}$ where $\alpha \simeq 2.67$ and $\sigma_0 \simeq 3.37 \times 10^{-20} \text{ cm}^2$ (Murphy & Yaqoob 2009; Tzanavaris et al. 2023).

Of course, our wind does not have a constant column-density. Instead this needs to be calculated separately for each wind cell. Making the simplifying assumption that the density within a single wind cell is roughly constant, we can write for the column-density in cell ij : $N_{H,ij} \simeq n_{ij} \Delta R_j$, where $\Delta R_j = r_j R_G d \log r$ is the radial width of the wind cell, and is directly calculated from the model geometry.

As we integrate radially along a sight-line θ_i , not only does the column-density evolve, but also the spectrum incident into the wind cell. For a given cell at (θ_i, r_j) , the incident spectrum $N(E)$ will be slightly absorbed by the cell at (θ_i, r_{j-1}) . Hence, the fluorescence from each cell is not simply calculated directly from Eqn. 10. Instead, we need to take into account the effect from *all* radially preceding cells on the incident spectrum, such that for a wind cell ij at (θ_i, r_j) , the incident spectrum is given by:

$$N_{ij}(E) = N(E) \prod_{k=1}^{j-1} \exp(-\sigma_{\text{Fe-K}}(E) A_{\text{Fe}} n_{ik} r_k d \log r R_G) \quad (11)$$

and so the fluorescence from the wind cell at ij is:

$$N_{\gamma,ij} = \frac{d \cos(\theta) d\phi}{4\pi} y \int_{E_K}^{\infty} (N_{ij}(E) - N_{i,j+1}(E)) dE \text{ photons s}^{-1} \text{ cm}^{-2} \quad (12)$$

which now also takes into account the solid angle of each wind cell as seen from the central source. In Eqn. 11, all factors

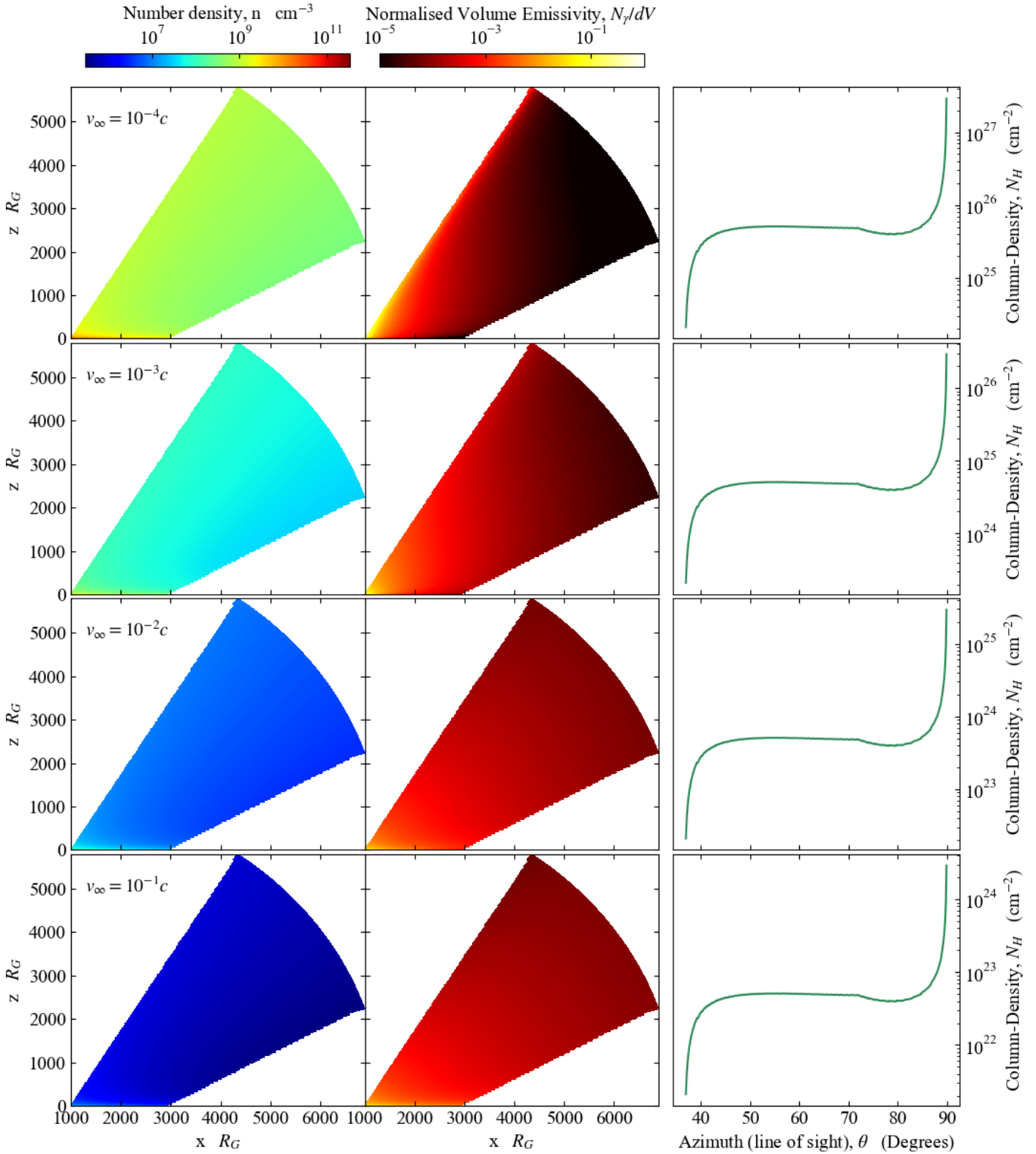


Fig. 2: Wind density profile (**left column**) and corresponding emissivity profile (**middle column**) for a range of outflow velocities (increasing from top to bottom, value given in top left corner of each row). The **right column** shows the column-density profile for varying lines-of-sight through the winds. These have all been calculated for a wind launched between $r_{\text{in}} = 1000$ and $r_{\text{out}} = 3000$, with $d_f = r_{\text{in}} \sqrt{3}$ and $f_{\text{cov}} = 0.9$. The mass outflow rate has been set to $\dot{m} = 0.1$, for a $10^8 M_{\odot}$ black hole (where the mass is required to obtain physical units). The velocity profile has been given a scale length of $r_v = 500$ and exponent $\beta = 1$, and the initial density profile (at the base) has $\kappa = -1$, weighting the outflow towards smaller radii. As expected, when the outflow velocity increases, the overall density also reduces. In general, the emissivity is weighted more strongly towards the base of the wind, where the density is highest (hence stronger absorption/fluorescence). For low velocity (high density), the emission will be strongly weighted to the inner edge of the wind, as now the absorption is sufficiently strong that the internal wind regions do not see significant illumination. Our highest velocity examples are chosen for demonstrative purposes rather than an attempt at a realistic BLR wind.

of M cancel (by expanding R_G and \dot{M}_{Edd}), such that the total fluorescence and line profile is fully independent of mass.

2.5. Calculating the overall line profile

The previous subsection only gives the emission in the co-moving frame of the wind. In the observes frame, the emission will be smeared out into a characteristic line shape. Material moving away/towards the observer will broaden the line due to Doppler shifts, the bulk outflowing motion of the wind will give a net blueshift, and relativistic length contraction and time-dilation will lead to a boosting effect in the emission originating from material travelling towards the observer. These are all very well known effects, which have previously been calculated for accretion discs (Chen et al. 1989; Fabian et al. 1989). In this section we give a generalisation to a 3D velocity profile, though *only in the weak field limit*.

In general, the energy of the emitted photon is given by the projection of the photon 4-momentum, p^α , onto the 4-velocity of the emitting material, u^α , such that $E_{\text{em}} = u_\alpha p^\alpha$ (Cunningham 1975; Luminet 1979). This will give the usual relation for the special relativistic Doppler shift in a flat space-time; as considered here.

The 4-velocity of the emitting material is simply given as $u_\alpha = g_{\alpha\beta} u^\beta = \gamma(c, -\mathbf{v}_w)$ where \mathbf{v}_w is the 3-velocity profile of the wind, $\gamma = (1 - (v_w/c)^2)^{-1/2}$ is the Lorentz factor of the wind material, and $g_{\alpha\beta}$ is the Minkowski metric. The wind 3-velocity components were previously calculated in section 2.2, such that in Cartesian coordinates:

$$u_\alpha = \gamma \{ c, -v_l \sin(\alpha) \cos(\phi) + v_\phi \sin(\phi), \\ -v_l \sin(\alpha) \sin(\phi) - v_\phi \cos(\phi), -v_l \cos(\alpha) \} \quad (13)$$

The 4-momentum of a photon is simply given by $p^\alpha = E_\gamma/c(1, \hat{\mathbf{n}}_\gamma)$, where $\hat{\mathbf{n}}_\gamma$ is a unit vector describing the direction of the photon. Energy is conserved along a trajectory, and so here $E_\gamma = E_{\text{obs}}$ (Cunningham 1975). Further, since we assume the photon travels in straight lines, the photon direction is simply $\hat{\mathbf{n}}_\gamma = (\sin(i), 0, \cos(i))$ for an observer located in the x-z plane at an inclination i from the z-axis. Hence, we arrive at the ratio between observed and emitted frame photon energies, *considering special relativity only*:

$$\frac{E_{\text{em}}}{E_{\text{obs}}} = \frac{u_\alpha p^\alpha}{E_{\text{obs}}} = \gamma \left\{ 1 - \frac{1}{c} \left[v_l \cos(\alpha) \cos(i) + \right. \right. \\ \left. \left. \sin(i) (v_l \sin(\alpha) \cos(\phi) - v_\phi \sin(\phi)) \right] \right\} \quad (14)$$

As expected, this is in the form of the special relativistic Doppler shift, except here it is decomposed into individual velocity components. Also factoring in the gravitational redshift, calculated in the Schwarzschild metric, gives:

$$\frac{E_{\text{em}}}{E_{\text{obs}}} = \gamma \left(1 - \frac{2}{r} \right)^{-\frac{1}{2}} \left\{ 1 - \frac{1}{c} \left[v_l \cos(\alpha) \cos(i) + \right. \right. \\ \left. \left. \sin(i) (v_l \sin(\alpha) \cos(\phi) - v_\phi \sin(\phi)) \right] \right\} \quad (15)$$

The above only gives the relation between emitted and observed photon energies. To relate this to an observed photon flux,

we take advantage of the fact that N_γ/E^3 is Lorentz invariant (Lindquist 1966; Cunningham 1975), such that:

$$N_{\gamma, \text{obs}} = \left(\frac{E_{\text{em}}}{E_{\text{obs}}} \right)^{-3} N_{\gamma, \text{em}} \\ \text{photons s}^{-1} \text{ cm}^{-2} \quad (16)$$

where $N_{\gamma, \text{em}}$ is calculated from Eqn. 12.

The total line-profile comes from integrating over the wind volume. However, as we do not know a priori what wind cells correspond to what specific energy shift, it is simpler to iterate over each cell, calculate the photon flux and energy shift from Eqns. 12, 15, and 16, adding the output photon flux to the relevant energy bin.

Throughout we use an internal fractional energy grid in E/E_0 , with bins evenly spaced from $E/E_0 = 0.2$ to 4.4 with $\Delta(E/E_0) = 2 \times 10^{-4}$. This allows for maximum velocity widths up to $0.9c$, which is more than adequate for any realistic wind. It also gives an internal energy resolution of 1.2 eV at 6 keV , oversampling that of XRISM-resolve ($\sim 5 \text{ eV}$ at 6 keV , Kelley et al. 2025).

As a sanity check, we apply our above methodology to a disc geometry, allowing for a direct comparison to DISKLINE (Fabian et al. 1989). This shows generally very good agreement for large radii, but begins to deviate systematically below $r \sim 50$ (see Appendix B, Fig. B.1). This is expected, since DISKLINE considers a treatment using the Schwarzschild metric (though no light-bending). *As such, we do not recommend the use of our model code for small launch radii.*

3. Model Properties

3.1. Emission Line Profiles

We illustrate the model emission line profiles in Fig. 3. We illustrate the effects by varying each parameter individually, while keeping the others fixed. The underlying fixed model is calculated for $\dot{m}_w = 10^{-2}$, $r_{\text{in}} = 1000$, $r_{\text{out}} = 3r_{\text{in}}$, $d_f = \sqrt{3}r_{\text{in}}$, $f_{\text{cov}} = 0.6$, $v_\infty = 10^{-3}$, $r_v = 100$, $\beta = 1$, and $\kappa = -1$. All line profiles have been normalised to unity, in order to highlight changes in the shape, and are observed at an inclination of 45 degrees.

To start, there is a clear trend in that the vast majority of the line profiles appear rather sharp. This is not surprising when we examine the emissivity profiles in Fig. 2. In general the emission is dominated by the inner edge at the base of the wind, as this is where both the density and incident flux is the strongest. At larger distances along the streamline, the density drops off, such that the absorption becomes less efficient, resulting in fewer photons available to re-emit. Alternatively, for lines of sight passing through a dense region (e.g at the base), the optical depth will be high, and so the incident continuum is mostly absorbed before it reaches the outer edge of the wind. This is clear in Fig. 3, which shows almost no change in the line profile when changing r_{out} .

In terms of understanding the physical origin of the wind, the key parameters are r_{in} , v_∞ and \dot{m}_w . The combination of r_{in} and v_∞ should inform the driving mechanism of the wind. Especially radiation driven outflow models, e.g UV line-driven winds (Proga et al. 2000; Proga & Kallman 2004), FRADO models (Czerny & Hryniwicz 2011; Naddaf et al. 2021), tend to have a specific radial range over which they can exist, as they strongly depend on the local disc SED, as well as containing predictions on the outflow velocity. As these both have significant impact on the line profile, they should be possible to constrain.

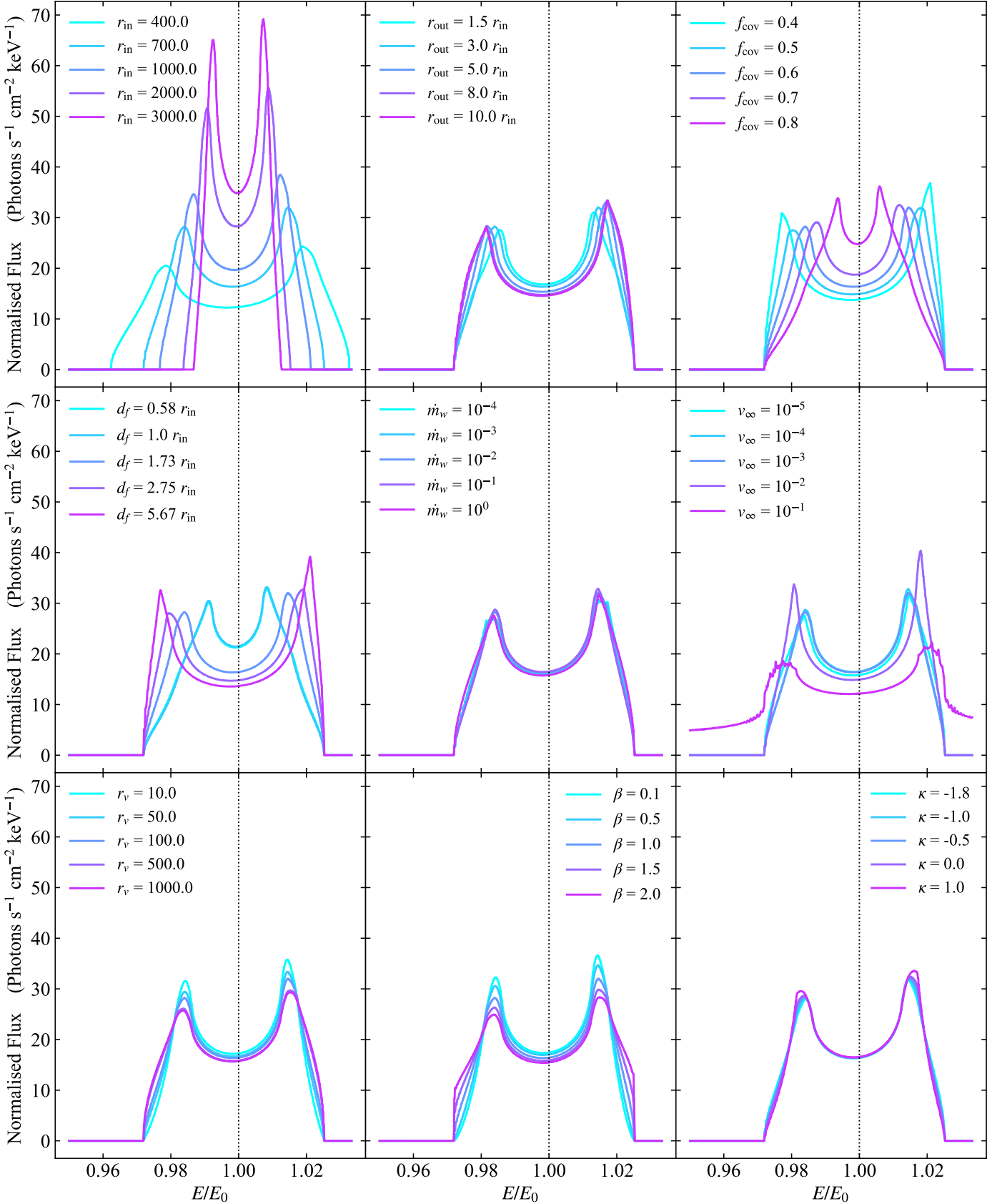


Fig. 3: Example emission line profiles and their evolution with varying wind parameters. These have all been re-normalised to have the same total flux, and have all been calculated for an observed inclination of 45 deg. Each panel shows the effect of varying an individual parameter, given in the top left corner of each panel. When not being varied, parameters are fixed at: $\dot{m}_w = 10^{-2}$, $r_{in} = 700$, $r_{out} = 3r_{in}$, $d_f = \sqrt{3}r_{in}$, $f_{cov} = 0.6$, $v_\infty = 10^{-3}$, $r_v = 100$, $\beta = 1$, $\kappa = -1$. These are all viewed at an observers inclination of $i = 45$ deg. The parameter choices for d_f are chosen such that they correspond to wind opening angles on the inner edge of $\alpha_{min} = 60^\circ, 45^\circ, 30^\circ, 20^\circ$, and 10° (see Fig. 1 for a definition of the opening angle).

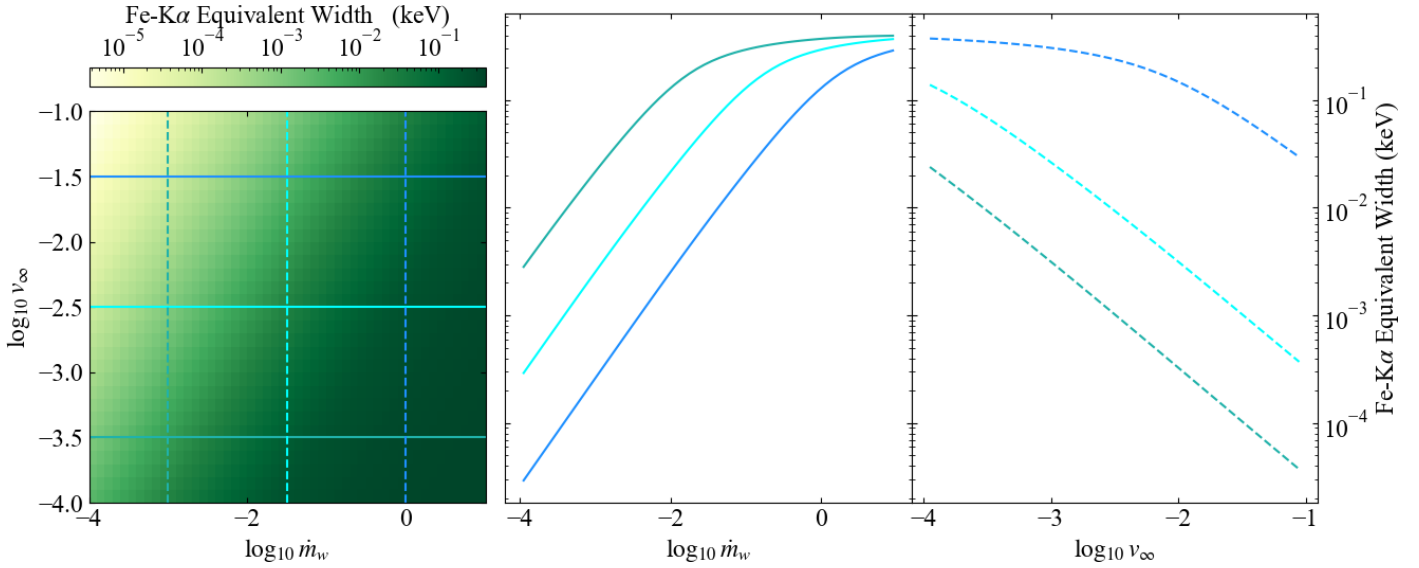


Fig. 4: **Left:** Colour-plot showing the equivalent width of the Fe-K α emission line for varying \dot{m}_w and v_∞ . The darker the shade of green, the larger the equivalent width. The vertical/horizontal solid/dashed lines correspond to the slices used to extract the curves of growth on the right as a function of \dot{m}_w/v_∞ .

Right: Curves of growth as a function of \dot{m}_w (left panel) and v_∞ (right panel). As \dot{m}_w increases, so does the equivalent width, until eventually the line saturates due to the wind going optically thick. Conversely, increasing v_∞ will reduce the equivalent width, as this reduces the overall density of the wind (see Fig. 2) leading to a lower degree of absorption and thus fewer photons available to re-emit as Fe-K α .

The behaviour of the line profile with v_∞ also reveals a key effect of calculating the density profile via mass-conservation. As one reduces the velocity, the overall density of the wind increases. In addition it appears from Fig. 2 that the moderate to high density regions also move further up the streamline. This will then increase the fraction of the emission originating from larger distances along a given streamline within the wind, which in turn traces a smaller angular velocity due to the conservation of angular momentum. The net effect is that the line profile begins to ‘fill in’ towards the centre.

3.2. Fe-K α Equivalent Width

A key advantage of our approach is that it gives a self-consistent normalisation to the Fe-K α emission line for a given wind density profile and incident X-ray spectrum (as also outlined in Tzanavaris et al. 2023). This depends strongly on both the mass-outflow rate, \dot{m}_w and outflow velocity profile (governed by v_∞), as these determine the density profile. We demonstrate this in Fig. 4. This shows on the left the expected equivalent width of the Fe-K α line for a grid of \dot{m}_w and v_∞ . On the right we show curves of growth with \dot{m}_w and v_∞ respectively. These are calculated for the same base model as the line-profiles in Fig. 3. The equivalent widths are calculated with respect to the incident continuum (a power-law, see section 2.4) at (rest-frame) 6.4 keV.

These behave as expected. Increasing \dot{m}_w leads to more material in the wind, and so naturally the density increases. Higher density leads to increased absorption of the incident spectrum, which in turn gives a higher number of available photons to re-emit. The perhaps more interesting effect is the saturation of the equivalent width once \dot{m}_w reaches a certain value. This is an effect of the wind going optically thick, and so now the limiting factor to the total fluorescence depends on the incident continuum rather than the wind density profile. However, increasing the normalisation of the incident continuum does not lead

to a higher equivalent width, as this is always measured relative to the continuum. Hence, we predict a rather stringent upper limit on the expected Fe-K α equivalent width from a wind of $EW \sim 5 \times 10^{-1}$ keV (for a covering fraction of 0.6. The exact value will naturally also depend somewhat on f_{cov}). This also becomes clear from Fig. 2 which shows how the emission becomes strongly concentrated to the inner edge of the wind when the density is sufficiently high, such that the incident spectrum is highly absorbed before reaching the inner/outer regions (top panel).

4. Application to XRISM data - a wind on the inner edge of the BLR in NGC 4151?

We demonstrate our model on a XRISM observation of NGC 4151, taken during the performance verification (PV) phase. NGC 4151 was observed five times during the PV phase (Xrism Collaboration et al. 2024; Xiang et al. 2025). We pick the longest observation to maximise signal-to-noise (obsID 300047020, observation date 18.05.2025, exposure time 103.7 ks, presented previously in Xiang et al. 2025).

Before constraining the line-profile, we also fit the broad-band continuum, using simultaneous XRISM-xtend (Noda et al. 2025a) and NuSTAR data. Below we give details on the data reduction, broad-band spectral fit, and finally our fit to the XRISM-resolve (Kelley et al. 2025) spectrum of the Fe-K α complex.

For all subsequent analysis, we use the reduction pipelines included in HEASOFT v.6.63, and XSPEC v.12.15.1 (Arnaud 1996). All errors are quoted at 90 % confidence.

4.1. XRISM-data reduction

We reduce both the XRISM-resolve and XRISM-xtend data, using the standard XRISM reduction pipeline along with the corresponding most recent calibration files from the CALDB database

(as of writing corresponding to the resolve and xtend calibration files from 15. September 2025, and the general files from 15 November 2024). We give here a brief overview of the reduction process, as also outlined in [Xrism Collaboration et al. \(2024\)](#).

We start by running `XAPIPELINE`, which generates the cleaned event files for both resolve and xtend. Next, focusing in XRISM-resolve, we use `XSELECT` to extract the source spectrum, filtering such that we *only* extract high-resolution primary (Hp) events. We also filter out periods of high particle background, and data from pixel 27 (as recommended due to a significant variation in gain). Using `RSLMKRMF` we then generate a RMF file, setting the size option to large (L) in order to accurately give the response around our region of interest (5-7 keV), but without the significant increase in file size that comes with including the electron loss continuum (the x-large option). For the ancillary response (ARF) file we first generate an exposure map using `XAXPMAP`, before then generating the ARF using `XAARFGEN`. Here we set the source type to a point-source, and run the ray-tracing of reflected and transmitted photons through the detector using 300000 photons.

For XRISM-xtend we extract a source spectrum from a rectangular region with dimensions $2.3'' \times 5.0''$ centred on the source. We then extract a background spectrum using the same extraction region, but on a portion of sky with no source contribution. The RMF file is generated using `XTDRMF`, and an ARF file in an identical manner to XRISM-resolve (but with the instrument set to xtend).

For both spectra, we bin the data such that each bin contains *at least* 25 counts, allowing for the use of χ^2 statistics during the fitting procedure.

4.2. NuSTAR data reduction

Simultaneous with the XRISM observation, NGC 4151 was observed by NuSTAR (obsID 60902010004, presented previously in [Xiang et al. 2025](#)). We combine these data with the XRISM-xtend data, to extend our broad-band continuum fit to 90.0 keV.

We use the standard `NUPipeline` tool to generate the cleaned event files, with `CALBD` calibration files corresponding to the most recent update as of writing (released 06 October 2025). After generating the cleaned event files, we run `NUPRODUCTS` to give both the source and background spectral files, the response file, and the ancillary response file; for both FPMA and FPMB modules. The source spectrum is extracted using a circular annulus with a radius of $120''$ centred on the source, while the background is extracted from an identical annulus in an empty patch of sky. As with the XRISM spectra, we re-bin the source spectrum to contain *at least* 25 counts per bin.

4.3. Broad-band spectral fit

Before constraining the profile of the Fe-K α complex we require an estimate of the underlying continuum. This is for two reasons. The first is that the intrinsic source continuum flux above ~ 7.1 keV determines the absolute strength of the Fe-K α fluorescence line (see Eqn. 10). The second is that broad features in the line profile are highly sensitive to the shape of the underlying continuum; especially if these features are weak.

Following Noda et al. (in prep) we construct a phenomenological model for the underlying continuum, using here the combined XRISM-xtend and NuSTAR data. At low energies below ~ 1.5 keV the XRISM-xtend spectrum is dominated by a complex scattered continuum. Hence, we limit the XRISM-xtend en-

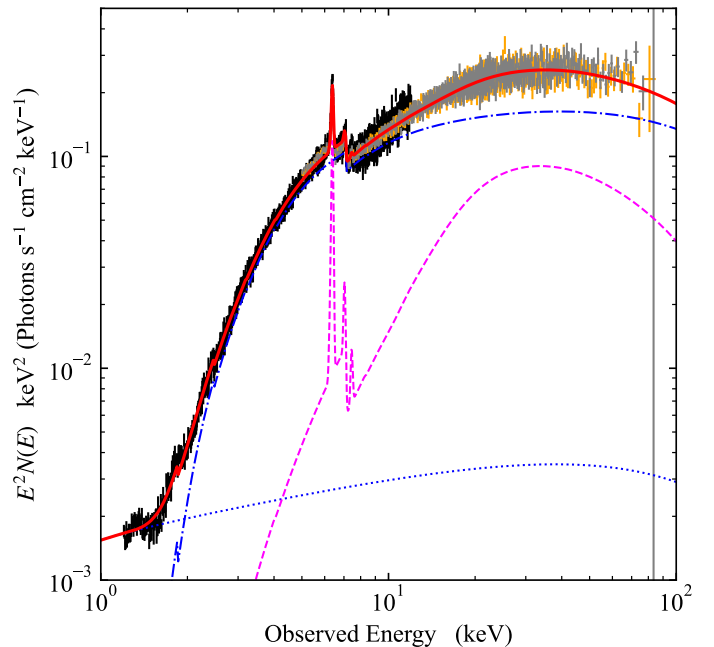


Fig. 5: Best fit broad-band continuum, using combined XRISM-xtend (black crosses) and NuSTAR (orange/grey crosses for FPMA/B respectively). The solid red line shows the total spectral model, with the dotted/dashed lines showing the individual components. These are: the scattered continuum (dotted blue), reflection spectrum (dashed magenta), and the primary continuum (dashed-dotted blue). The plotted NuSTAR data have been corrected by a cross-calibration constant used to account for instrumental differences between XRISM-xtend and NuSTAR. The data have been re-binned slightly for clarity.

ergy range to $1.2 - 12$ keV during the fitting, where we note that part of the scattered continuum is included in order to estimate its contribution to the overall flux level. For NuSTAR, we consider the energy range between $5.0-90.0$ keV; giving a total combined band-pass of $1.2-90$ keV. The total source spectrum is shown in Fig. 5.

To describe the primary continuum we use a redshifted cut-off power-law (`ZCUTOFFPL` in `XSPEC`), subject to absorption from the host galaxy (`TBABS` [Wilms et al. 2000](#)) and also partial covering absorption intrinsic to the AGN itself (e.g from a wind) (`PCfabs`). We then include a component originating from cold reflection off the disc (`PEXMON` [Magdziarz & Zdziarski 1995](#); [Nandra et al. 2007](#)) convolved with Gaussian broadening (`GSMOOTH`) to account for the iron emission and Compton hump. Here we fix the observer inclination at 60 degrees and all abundances to solar abundances. Finally, we include an additional cut-off power-law, with photon index and cut-off energy tied to the primary continuum, to describe the scattered continuum. The total model is then also absorbed by our galaxy, where we fix $N_H = 2 \times 10^{20} \text{ cm}^{-2}$. The final `XSPEC` model is then: $\text{TBABS}_{\text{MW}} * (\text{ZCUTOFFPL}_{\text{scatt}} + \text{TBABS}_{\text{int}} * (\text{PCfabs} * \text{ZCUTOFFPL}_{\text{primary}} + \text{GSMOOTH} * \text{PEXMON}))$. We also include a cross-calibration constant, applied to the NuSTAR data, to account for small calibration differences between XRISM-xtend and NuSTAR.

This gives a moderate fit to the broad-band spectrum, with $\chi^2_v = 4876/3760 = 1.3$. The increase in χ^2 is predominantly being driven by complexity in the scattered continuum, and in the region $5 - 8$ keV where details in the Fe-K α profile not captured by this model as well as absorption lines (as seen in

Component	Parameter (Unit)	Value
TBABS _{MW}	N_H (10 ²² cm ⁻²)	0.02
ZCUTOFFPL _{scatt}	Γ	1.71 ^{+0.02} _{-0.01}
	E_{cut} (keV)	132 ⁺¹⁸ ₋₁₂
	Norm.	0.00165 ^{+4e-05} _{-2e-05}
TBABS _{int}	N_H (10 ²² cm ⁻²)	6.2 ^{+0.2} _{-0.1}
PCFABS	N_H (10 ²² cm ⁻²)	14.7 ^{+1.4} _{-0.5}
	f_{cov}	0.59 ^{+0.01} _{-0.02}
ZCUTOFFPL _{primary}	Γ	= Γ_{scatt}
	E_{cut} (keV)	= $E_{\text{cut,scatt}}$
	Norm.	0.077 ^{+0.004} _{-0.002}
GSMOOTH	$\sigma_{6\text{ keV}}$	0.044 ^{+0.005} _{-0.008}
	Index	1
PEXMON	Γ	= Γ_{scatt}
	E_{cut} (keV)	= $E_{\text{cut,scatt}}$
	Relative Reflection	-1
	Abund.	1
	A_{Fe}	1
Const _{NuSTAR}	Inc. (deg)	60
		1.072 ^{+0.005} _{-0.005}
Redshift		0.003326
$\chi^2/\text{d.o.f}$		4876.56/3760 = 1.3

Table 1: Best fit parameters to the broad-band fit of the XRISM-xtend and NuSTAR data, using the model: TBABS_{MW} * (ZCUTOFFPL_{scatt} + TBABS_{int} * (PCFABS * ZCUTOFFPL_{primary} + GSMOOTH * PEXMON)). These have all been calculated from an MCMC chain, in XSPEC, using 8 walkers and 160000 steps. The errors correspond to 90 % confidence. Parameter values prefixed with an = are tied to the given component. The constant is included to account for calibration differences between XRISM-xtend and NuSTAR.

Xiang et al. 2025) not included here drive significant residuals. As these are a known effect, and since the broad-band continuum shape is otherwise well constrained, we continue with this as our underlying base continuum for our more detailed analysis of the XRISM-resolve spectrum in the next subsection. The best fit continuum model is shown in Fig. 5, with corresponding fit parameters shown in Table 1. The errors are estimated at 90 % confidence from a MCMC chain using 8 walkers and 160000 steps.

4.4. Model application to XRISM-resolve

We now focus our analysis onto the XRISM-resolve spectrum. Specifically, we focus on the shape of the Fe-K α complex, and so limit the spectral fit to the energy range 5.0 – 6.6 keV (in the observed frame).

For the underlying continuum we take the model from the broad-band spectral fit, fixing all parameters to those in Table 1. We make one change, removing the RDBLUR*PEXMON component, as we are now focusing on a detailed fit of the Fe-K α complex. Xrism Collaboration et al. (2024) showed three distinct components to the Fe-K α line, which we adapt here. We start with a MYTORUS (Yaqoob 2012) component, convolved with RDBLUR (Fabian et al. 1989), to account for the narrow Torus emission. Specifically, we use the updated MYTORUS line emission files (mytl_V000HLZnEp000_v01.fits) from Yaqoob (2024) as these include the intrinsic Fe-K α profile from Hölzer et al. (1997). In RDBLUR we fix the emissivity index to -2, in order to account for the non-disc geometry of the torus, and set a lower limit of 10⁴ R_G for the inner radius. We fix the outer radius at 10⁷ R_G .

Next we add a XWINDFE component, to account for the moderately broad BLR scale emission; the main focus of this analysis. We stress that XWINDFE will self-consistently calculate the equivalent width of the line for a given input spectrum, and also includes the intrinsic Hölzer et al. (1997) profile for the rest-frame emission (see section 2 for a full model description). Hence we tie the input spectrum for XWINDFE to that of the primary continuum in the broad-band fit. We also fix a number of the geometric parameters in order to simplify the fit. Firstly, we set the outer launch radius to $r_{\text{out}} = 1.5r_{\text{in}}$, since we are aiming to describe a wind on the inner edge of the BLR, and so this will in effect limit the radial extent of the wind. Secondly, we fix $d_f = r_{\text{in}}\sqrt{3}$, effectively fixing the opening angle on the inner edge to $\alpha_{\text{min}} = 30^\circ$ (see Fig. 1). In the geometry considered here this also sets an upper limit on the covering fraction of $f_{\text{cov,max}} \simeq 0.86$. From Fig. 3 we see that the velocity parameters r_v and β , as well as the radial launch efficiency parameter κ , have only a small impact on the overall line shape. Hence we fix these at $r_v = 200$, $\beta = 1$, and $\kappa = -1$, as typically done for radiative winds (e.g Matzeu et al. 2022). During initial fitting attempts we also noted that the fit was insensitive to the turbulent velocity v_{turb} , hence we fix this at 0 (where the choice is motivated by the fact that this allows the code to skip an additional convolution step, speeding up the fit). We also fix all abundances to their solar values, using the values from Anders & Grevesse (1989).

Finally, we include a DISKLINE (Fabian et al. 1989) component, to account for the presence of an inner accretion disc. We allow the inner radius to be free, but fix the outer radius to 10³ R_G . We also fix the emissivity index to -3, as expected for a flat disc.

Thus, the final XSPEC model is: TBABS_{MW} * (ZCUTOFFPL_{scatt} + TBABS_{int} * (PCFABS * ZCUTOFFPL_{primary} + RDBLUR * MYTORUS + ZASHIFT * (XWINDFE + DISKLINE))), where the ZASHIFT component accounts for the lack of a redshift parameter in both XWINDFE and DISKLINE. In Appendix C we test the effect of removing individual model components to the Fe-K α complex in order to assess their significance to the overall fit.

This gives an excellent fit to the 5.0–6.6 keV XRISM-resolve spectrum, with a $\chi^2_y = 2134/2067 = 1.03$. The resulting fit parameters are given in table 2, and the spectrum is shown in Fig 6, where we have elected to only show the 6.0–6.6 keV range in order to highlight the Fe-K α complex.

The resulting XWINDFE parameters suggest a slow-moving ($\log_{10}(v_{\infty}/c) \simeq -3.5$) wind with a moderately low mass-outflow rate ($\log_{10} \dot{m}_w \simeq -3.0$). Specifically the mass-outflow rate is important, as this is significantly lower than the accretion rate for NGC 4151 ($\dot{m} \sim 0.02$, Mahmoud & Done 2020), indicating that although the impact on the line-profile is significant, this slow wind's impact to the accretion flow will likely be minimal. In

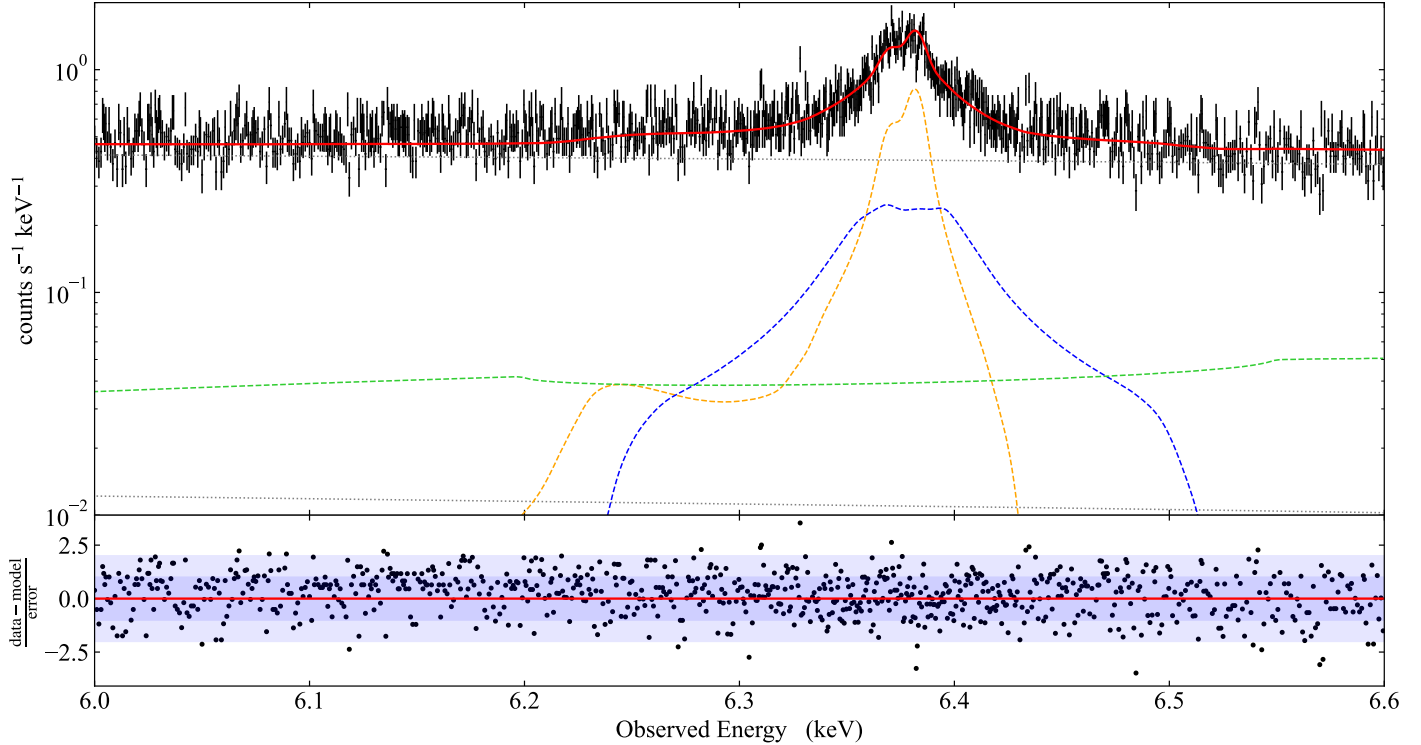


Fig. 6: **Top:** Best fit model to XRISM-resolve data (black points). The solid red line shows the total model, while the dashed and dotted lines show the components. These are: scattered and primary continuum (grey dotted lines), MYTORUS emission line from Compton thick slow moving material (orange dashed line), xwindfe emission line for a wind inwards of the BLR (blue dashed line), and DISKLINE emission line from the inner disc (green dashed line). **Bottom:** Data-model residuals, normalised by the data errorbar. The shaded blue bands show the 1σ (dark) and 2σ (light) deviation.

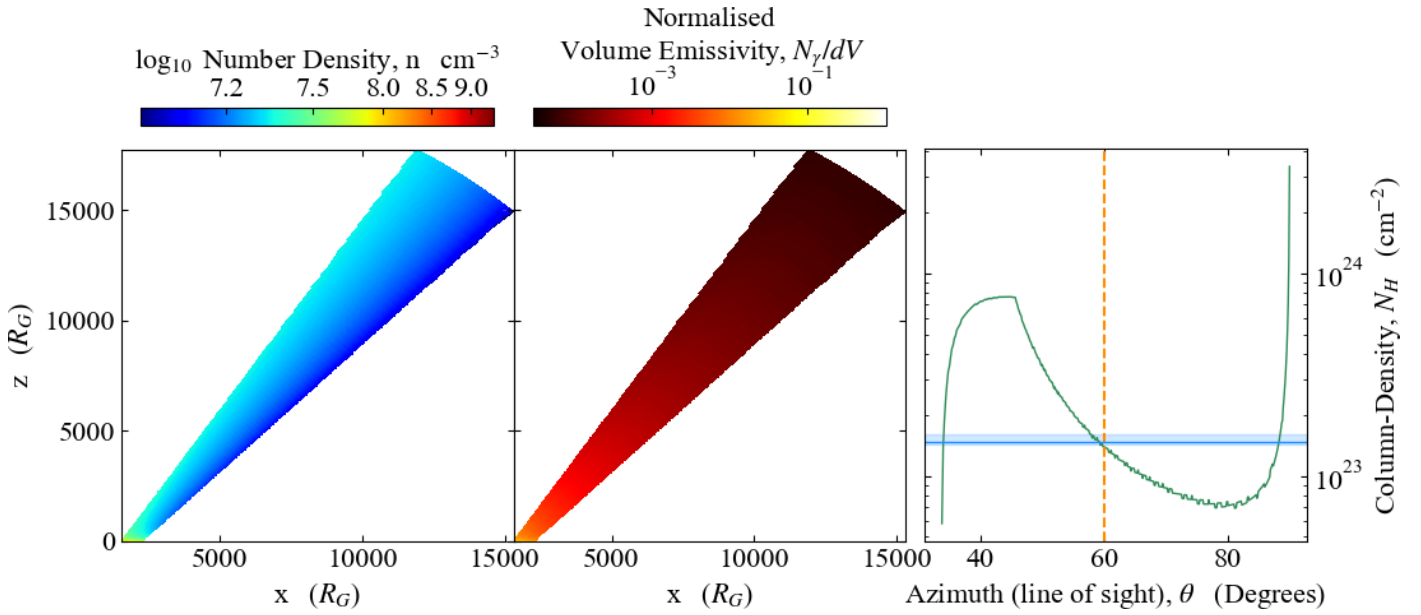


Fig. 7: **Left and Middle:** Wind density (left) and emissivity (right) profiles corresponding to the best fit xwindfe model fit to the XRISM-resolve data (Fig. 6). It is clear that the high density and emissivity regions are concentrated towards the base of the wind. However, some additional contribution from larger scale regions in the wind contribute to giving the 'narrow-er' core seen in the line profile in Fig. 6. **Right:** Column-density profile as a function of azimuth through the wind (green line). The drop at $\sim 50^\circ$ corresponds to the point where sight-lines do not reach the outer radius of the wind, rather cutting through the central regions. The vertical dashed orange line indicates the observer inclination for NGC 4151, while the solid blue horizontal line indicates the column-density of the PCFABS component as inferred from the continuum fit. The agreement here is remarkable given that the xwindfe fit did not use any prior constraints on line-of-sight column-density.

some sense this is reassuring, given the near ubiquitous presence of a BLR across the AGN population.

The inferred outflow velocity, $v_\infty/c \simeq 10^{-3.5} \simeq 100 \text{ km s}^{-1}$, however does appear rather low. Especially given that the escape velocity at $r_{\text{in}} \simeq 1550$ is $v_{\text{esc}} \sim 7600 \text{ km s}^{-1}$. This is likely because our model *only* considers outflowing material in a wind geometry. More realistic BLR geometries are probably multi-component, with a non-outflowing virialized component and potentially also an inflowing component. Indeed, the physically motivated FRADO models Czerny & Hryniec (2011) for the BLR give material that first rises in a dusty wind, before failing and falling back towards the disc. As such, we caution the reader that assuming the entire BLR can be modelled with xwind, as done here for demonstrative purposes, is likely physically incomplete, and a more realistic picture could be obtained by including some contribution from non-outflowing material. However, this is beyond the scope of this paper, where we instead note that xwind does give a physically motivated method for adding in a wind component to the BLR emission. Additionally, Kraemer et al. (2006) does suggest that this wind component should be present, as seen through slow moving, $\sim 500 \text{ km s}^{-1}$, material seen in absorption.

More interesting in terms of the wind itself is the resulting density profile, as seen in Fig. 7. Initially, one would think that the low outflow rate would give a relatively low density. However, this is counteracted by the low outflow velocity, giving instead a moderate density range of $\sim 10^7 - 10^9 \text{ cm}^{-3}$. While the high density regions are concentrated towards the base of the wind, the larger scale regions appear to have a relatively uniform profile, with $n \sim 10^{7.2} - 10^{7.5} \text{ cm}^{-3}$. This impacts the line-profile, allowing for significant emission from spatial scales well beyond the base, giving the smooth 'narrowing' of the emission line seen in Fig. 6. However, it is uncertain whether all of this 'large spatial scale' emission is genuinely present, and not simply a fitting degeneracy due to a lack of a non-outflowing component to the BLR. Nonetheless, we note that the derived density profile gives a line-of-sight column-density of $N_H \sim 1.4 \times 10^{23} \text{ cm}^{-2}$, in surprisingly close agreement of the $1.47^{+0.14}_{-0.05} \times 10^{23} \text{ cm}^{-2}$ derived for the partial covering absorber in the continuum fit with XRISM-Xtend and NuSTAR. This adds confidence that the derived model geometry is physically consistent with the observed X-ray absorption.

5. Discussion and Conclusions

We have developed a model for the emission line profiles originating from a wind structure at BLR like scales, xwind, which we have made publicly available. Our approach gives a physically motivated model that can easily be fit to XRISM data, and in the future NewAthena.

There are a number of caveats. Perhaps the most important being that we assume neutral material. This is unlikely to be the case for material surrounding an AGN, given the highly ionising SED typically associated with the inner accretion flow. Given the wide range in wind density, one might expect a range of ionisation states throughout. This should affect the line profile, as even small changes in ionisation can shift or weaken the emitted line (e.g. Bianchi et al. 2005), which would in the best case simply mildly smooth the line, in the worst case significantly alter the line shape. The magnitude of these effects should depend on wind properties, placing some limits to model parameters within which the results can be trusted. While we do not calculate ionisation on the fly, we can make a rough estimate. Using the SED of NGC 4151 from Mahmoud & Done (2020) and the wind den-

sities derived in Section 4.4 we arrive at ionisation parameters ranging from $\log_{10} \xi \sim 2.5 - 3.5$ in the high emissivity regions, where $\xi = L_{\text{ion}}/(n_H R^2)$ and L_{ion} is the integrated luminosity from 13.6 eV to 13.6 keV (1–1000 Ryd); following standard definitions (Ferland et al. 2017; Mehdipour et al. 2016). This is initially problematic, given that in this regime one expects a significant contribution from ionised species of iron (Mehdipour et al. 2016). But this is neglecting clumping, which could increase the local density of the emitting material, and thus reduce the overall ionisation state. XRISM Collaboration et al. (2025) showed conclusively a clumpy outflow in PDS 456 through absorption, although that is for a UFO wind where the models of Matzeu et al. (2022) and Luminari et al. (2024) are likely more appropriate. However, it would not be unreasonable to assume that clumping can extend to these slower BLR scale winds. Especially given the presence of the low ionisation slow moving absorption lines seen in Kraemer et al. (2006). As such we caution the reader that this model is a first order approximation. Both in terms of ignoring internal clumping, such that xwind can be thought of as a volume-averaged approximation, and in terms of the ionisation state of the material which is completely ignored. While increasing the local density through clumping can address *some* of the caveats, we caution that this model *should not* be used for material significantly inwards of the BLR ($r \lesssim 1000$) where ionisation will almost certainly alter the line shape.

There is also the caveat of the simplified geometry and velocity profile. We have assumed that the material is always outflowing. However this is likely not the case, especially given the rather low outflow velocity derived in section 4. It may be expected that at some point the outflow fails and the material falls back down, as in e.g. the failed radiative outflow models of the BLR (Czerny & Hryniec 2011; Naddaf et al. 2021). The motion of this infalling material is likely to be somewhat more chaotic than the smooth outflowing wind assumed here, potentially providing some additional smoothing or narrow component to the model line profile. Of course, the total effect of this would depend somewhat of the column-density of the intervening wind, as the wind inwards of this would still cast a shadow across any material falling back down. Nonetheless, we caution that a physically complete picture should include at least a non outflowing component, and that xwind only provides a method for adding in the wind.

Caveats aside, the model does give a statistically good fit to the data, while providing physical constraints on BLR like winds. It is particularly promising that our model fits not only give launch radii consistent with that seen in previous XRISM analysis of NGC 4151 (XRISM Collaboration et al. 2024; Xiang et al. 2025), but also provides reasonable mass-outflow rates compared to the mass-accretion rate for NGC 4151. Though we stress that this is only one viable explanation, and that there are likely other models that give equally good fits to these data.

XRISM has provided an unprecedented view of the X-ray emitting regions in astrophysical sources, and for AGN has allowed for the characterisation of multiple components to the Fe-K α emitting regions. These data are of sufficient quality that they warrant physical models, in order to start characterising their actual structure. Our approach provides a step forward in this regard, giving a fast and simple, yet physical, model for BLR scale outflows. In the future we will start applying our model to a wider sample of XRISM observations of moderately accreting AGN, with the aim of understanding the structure of BLR like outflows across the wider population.

Component	Parameter (Unit)	Value
RDBLUR	Index	-2
	$r_{\text{in}} (R_G)$	13074^{+26760}_{-2178}
	$r_{\text{out}} (R_G)$	10^7
MYTORUS	$N_H 10^{24} \text{ cm}^{-2}$	$9.1^{+0.5}_{-6.4}$
	Γ^\dagger	1.7103
	Norm.	$0.08^{+0.01}_{-0.02}$
XWINDFE	$\log_{10} \dot{m}_w$	$-3.0^{+0.8}_{-1.3}$
	$r_{\text{in}} (R_G)$	1549^{+837}_{-258}
	$r_{\text{out}} (R_G)$	$= 1.5 r_{\text{in}}$
	$d_f (R_G)$	$= r_{\text{in}} \sqrt{3}$
	$f_{\text{cov}} \left(\frac{\Omega}{4\pi} \right)$	$0.83^{+0.01}_{-0.05}$
	$\log_{10} v_\infty (c)$	$-3.5^{+0.7}_{-1.4}$
	$r_v (R_G)$	200
	β	1
	$v_{\text{turb}} (\text{km/s})$	0
DISKLINE	κ	-1
	$A_{\text{Fe}} ([\text{Fe}]/[\text{Fe}_\odot])$	1
	N_0^*	0.0766176
	Γ^\dagger	1.7103
	$E_0 (\text{keV})$	6.4
	Index	-3
Inc. (deg)	$r_{\text{in}} (R_G)$	$25.5^{+12.4}_{-8.3}$
	$r_{\text{out}} (R_G)$	10^3
	Norm.	$0.00050^{+9e-05}_{-7e-05}$
	Redshift	0.003326
$\chi^2/\text{d.o.f}$		2133.8/2067 = 1.03

Table 2: Best fit parameters for the model fit to the Fe- $\text{K}\alpha$ complex in the XRISM-Resolve spectrum. The continuum parameters are not shown here, since they are previously given in table 1. The errors correspond to 90 % confidence intervals, calculated from an MCMC chain run for 160 000 steps.

[†] fixed to Γ_{primary} in table 1.

^{*} fixed to Norm_{primary} in table 1.

Acknowledgements. We thank the anonymous referee for their constructive comments, which improved the quality of this manuscript. We would like to thank the XRISM team for their work on the initial compilation and analysis of the high resolution data, which motivated this work. We would also like to thank Jon M. Miller for useful discussions, in particular on the NGC 4151 data. SH acknowledges support from an IFPU fellowship, as well as previous support from the Science and Technologies Facilities Council (STFC) through the studentship ST/W507428/1. CD acknowledges support from STFC through the grant ST/T000244/1.

This work made use of the following software: XSPEC (Arnaud 1996), NUMPY

(Harris et al. 2020), ASTROPY (Astropy Collaboration et al. 2013, 2018, 2022), and meson.

Code availability

The xwind model code is available via the corresponding author's GitHub page (<https://github.com/scotthgn>). We release two version. One written exclusively in FORTRAN designed to be used with the xspec spectral fitting package (<https://github.com/scotthgn/XWIND>), and a PYTHON version designed to give more flexibility (and plotting options), referred to as PYXWIND (<https://github.com/scotthgn/PyXWIND>).

Data availability

Both the XRISM and NuSTAR data are publicly available via the HEASARC service, and were previously published in Xiang et al. (2025).

References

Anders, E. & Grevesse, N. 1989, *Geochim. Cosmochim. Acta*, 53, 197
 Andonie, C., Bauer, F. E., Carraro, R., et al. 2022a, *A&A*, 664, A46
 Andonie, C., Ricci, C., Paltani, S., et al. 2022b, *MNRAS*, 511, 5768
 Arnaud, K. A. 1996, in *Astronomical Society of the Pacific Conference Series*, Vol. 101, *Astronomical Data Analysis Software and Systems V*, ed. G. H. Jacoby & J. Barnes, 17
 Astropy Collaboration, Price-Whelan, A. M., Lim, P. L., et al. 2022, *ApJ*, 935, 167
 Astropy Collaboration, Price-Whelan, A. M., Sipócz, B. M., et al. 2018, *AJ*, 156, 123
 Astropy Collaboration, Robitaille, T. P., Tollerud, E. J., et al. 2013, *A&A*, 558, A33
 Begelman, M. C. & McKee, C. F. 1983, *ApJ*, 271, 89
 Begelman, M. C., McKee, C. F., & Shields, G. A. 1983, *ApJ*, 271, 70
 Behar, E. 2009, *ApJ*, 703, 1346
 Bianchi, S., La Franca, F., Matt, G., et al. 2008, *MNRAS*, 389, L52
 Bianchi, S., Miniutti, G., Fabian, A. C., & Iwasawa, K. 2005, *MNRAS*, 360, 380
 Bischetti, M., Fiore, F., Feruglio, C., et al. 2023, *ApJ*, 952, 44
 Bischetti, M., Maiolino, R., Carniani, S., et al. 2019, *A&A*, 630, A59
 Bischetti, M., Piconcelli, E., Vietri, G., et al. 2017, *A&A*, 598, A122
 Blandford, R. D. & Payne, D. G. 1982, *MNRAS*, 199, 883
 Bogensberger, D., Nakatani, Y., Yaqoob, T., et al. 2025, *PASJ*, 77, S209
 Chen, K., Halpern, J. P., & Filippenko, A. V. 1989, *ApJ*, 339, 742
 Choi, H., Leighly, K. M., Terndrup, D. M., et al. 2022, *ApJ*, 937, 74
 Choi, H., Leighly, K. M., Terndrup, D. M., Gallagher, S. C., & Richards, G. T. 2020, *ApJ*, 891, 53
 Cunningham, C. T. 1975, *ApJ*, 202, 788
 Czerny, B. & Hryniewicz, K. 2011, *A&A*, 525, L8
 De Rosa, G., Peterson, B. M., Ely, J., et al. 2015, *ApJ*, 806, 128
 Dehghanian, M., Ferland, G. J., Kriss, G. A., et al. 2019a, *ApJ*, 877, 119
 Dehghanian, M., Ferland, G. J., Peterson, B. M., et al. 2019b, *ApJ*, 882, L30
 Elvis, M., Wilkes, B. J., McDowell, J. C., et al. 1994, *ApJS*, 95, 1
 Fabian, A. C., Rees, M. J., Stella, L., & White, N. E. 1989, *MNRAS*, 238, 729
 Ferland, G. J., Chatzikos, M., Guzmán, F., et al. 2017, *Rev. Mexicana Astron. Astrofis.*, 53, 385
 Feruglio, C., Fiore, F., Carniani, S., et al. 2015, *A&A*, 583, A99
 Fiore, F., Feruglio, C., Shankar, F., et al. 2017, *A&A*, 601, A143
 Fukumura, K., Kazanas, D., Contopoulos, I., & Behar, E. 2010, *ApJ*, 715, 636
 Fukumura, K., Kazanas, D., Shrader, C., et al. 2017, *Nature Astronomy*, 1, 0062
 GRAVITY Collaboration, Amorim, A., Bourdarot, G., et al. 2024, *A&A*, 684, A167
 GRAVITY+ Collaboration, El Dayem, K. A., Aimar, N., et al. 2025, *arXiv e-prints*, arXiv:2509.13911
 Haardt, F. & Maraschi, L. 1993, *ApJ*, 413, 507
 Haardt, F., Maraschi, L., & Ghisellini, G. 1994, *ApJ*, 432, L95
 Hagino, K., Odaka, H., Done, C., et al. 2015, *MNRAS*, 446, 663
 Hagino, K., Odaka, H., Done, C., et al. 2016, *MNRAS*, 461, 3954
 Harris, C. R., Millman, K. J., van der Walt, S. J., et al. 2020, *Nature*, 585, 357
 Higginbottom, N., Knigge, C., Long, K. S., et al. 2018, *MNRAS*, 479, 3651
 Hölzer, G., Fritsch, M., Deutsch, M., Härtwig, J., & Förster, E. 1997, *Phys. Rev. A*, 56, 4554
 Igo, Z., Parker, M. L., Matzeu, G. A., et al. 2020, *MNRAS*, 493, 1088

Kammoun, E., Kawamuro, T., Murakami, K., et al. 2025, *ApJ*, 994, L13

Kara, E., Mehdić, M., Kriss, G. A., et al. 2021, *ApJ*, 922, 151

Kelley, R. L., Ishisaki, Y., Costantini, E., et al. 2025, *Journal of Astronomical Telescopes, Instruments, and Systems*, 11, 042026

King, A. R. 2010, *MNRAS*, 402, 1516

Knigge, C., Woods, J. A., & Drew, J. E. 1995, *MNRAS*, 273, 225

Kraemer, S. B., Crenshaw, D. M., Gabel, J. R., et al. 2006, *ApJS*, 167, 161

Leighly, K. M., Hamann, F., Casebeer, D. A., & Grupe, D. 2009, *ApJ*, 701, 176

Leighly, K. M., Terndrup, D. M., Gallagher, S. C., Richards, G. T., & Dietrich, M. 2018, *ApJ*, 866, 7

Lindquist, R. W. 1966, *Annals of Physics*, 37, 487

Long, K. S. & Knigge, C. 2002, *ApJ*, 579, 725

Luminari, A., Nicastro, F., Krongold, Y., Piro, L., & Thakur, A. L. 2023, *A&A*, 679, A141

Luminari, A., Piconcelli, E., Tombesi, F., Nicastro, F., & Fiore, F. 2024, *A&A*, 691, A357

Luminari, A., Piconcelli, E., Tombesi, F., et al. 2018, *A&A*, 619, A149

Luminet, J. P. 1979, *A&A*, 75, 228

Lusso, E. & Risaliti, G. 2016, *ApJ*, 819, 154

Magdziarz, P. & Zdziarski, A. A. 1995, *MNRAS*, 273, 837

Mahmoud, R. D. & Done, C. 2020, *MNRAS*, 491, 5126

Maiolino, R., Gallerani, S., Neri, R., et al. 2012, *MNRAS*, 425, L66

Matthews, J. H., Long, K. S., Knigge, C., et al. 2025, *MNRAS*, 536, 879

Matzeu, G. A., Lieu, M., Costa, M. T., et al. 2022, *MNRAS*, 515, 6172

Matzeu, G. A., Reeves, J. N., Braito, V., et al. 2017, *MNRAS*, 472, L15

Mehdić, M., Kaastra, J. S., Eckart, M. E., et al. 2025, *A&A*, 699, A228

Mehdić, M., Kaastra, J. S., & Kallman, T. 2016, *A&A*, 596, A65

Miller, J. M., Cackett, E., Zoghbi, A., et al. 2018, *ApJ*, 865, 97

Miller, J. M., Xiang, X., Byun, D., et al. 2025, *ApJ*, 994, L10

Murphy, K. D. & Yaqoob, T. 2009, *MNRAS*, 397, 1549

Naddaf, M.-H., Czerny, B., & Szczepański, R. 2021, *ApJ*, 920, 30

Nandra, K., O'Neill, P. M., George, I. M., & Reeves, J. N. 2007, *MNRAS*, 382, 194

Nardini, E., Reeves, J. N., Gofford, J., et al. 2015, *Science*, 347, 860

Noda, H., Mineta, T., Minezaki, T., et al. 2023, *ApJ*, 943, 63

Noda, H., Mori, K., Tomida, H., et al. 2025a, *PASJ*, 77, S10

Noda, H., Yamada, S., Ogawa, S., et al. 2025b, *ApJ*, 993, L53

Nomura, M. & Ohsuga, K. 2017, *MNRAS*, 465, 2873

Nomura, M., Ohsuga, K., Takahashi, H. R., Wada, K., & Yoshida, T. 2016, *PASJ*, 68, 16

Odaka, H., Aharonian, F., Watanabe, S., et al. 2011, *ApJ*, 740, 103

Proga, D. & Kallman, T. R. 2004, *ApJ*, 616, 688

Proga, D., Stone, J. M., & Kallman, T. R. 2000, *ApJ*, 543, 686

Reeves, J. N., O'Brien, P. T., Braito, V., et al. 2009, *ApJ*, 701, 493

Shakura, N. I. & Sunyaev, R. A. 1973, *A&A*, 24, 337

Sim, S. A., Long, K. S., Miller, L., & Turner, T. J. 2008, *MNRAS*, 388, 611

Tombesi, F., Cappi, M., Reeves, J. N., et al. 2010, *A&A*, 521, A57

Tzanavaris, P., Yaqoob, T., & LaMassa, S. 2023, *Phys. Rev. D*, 108, 123037

Vander Meulen, B., Camps, P., Stalevski, M., & Baes, M. 2023, *A&A*, 674, A123

Weymann, R. J., Morris, S. L., Foltz, C. B., & Hewett, P. C. 1991, *ApJ*, 373, 23

Wilms, J., Allen, A., & McCray, R. 2000, *ApJ*, 542, 914

Xiang, X., Miller, J. M., Behar, E., et al. 2025, *ApJ*, 988, L54

Xrism Collaboration, Audard, M., Awaki, H., et al. 2024, *ApJ*, 973, L25

Xrism Collaboration, Audard, M., Awaki, H., et al. 2025, *Nature*, 641, 1132

Yaqoob, T. 2012, *MNRAS*, 423, 3360

Yaqoob, T. 2024, *MNRAS*, 527, 1093

Yaqoob, T., George, I. M., Nandra, K., et al. 2001, *ApJ*, 546, 759

Yaqoob, T. & Padmanabhan, U. 2004, *ApJ*, 604, 63

Appendix A: xwind model documentation

We release both an xspec version of xwind, written in FORTRAN, as well as a stand-alone PYTHON version, PYXWIND, for use-cases outside of xspec. Within xwind we release three model flavours: xwindline, xwindfe, and xwindconv. Here we give a brief overview of each model flavour. We note that PYXWIND includes additional functionality for plotting and the calculation of column-density profiles. For these details we refer the reader to the documentation on the GitHub page: <https://github.com/scotthgn/PyXWIND>.

xwindline: This is the base model, which simply focuses on the line-shape as given by the wind. As such the rest-frame energy is treated as a free parameter, and the rest-frame emission is considered a simple delta-function. Here the normalisation should also be treated as a free parameter, as the model does not consider the output equivalent width. The input parameters for xwindline are given in table A.1.

xwindfe: This model is specific to the Fe-K α complex. As such it calculates self-consistently the equivalent width of the emission line (see section 3.2), and so the normalisation in xspec should *always* be fixed at unity. The absolute line flux is instead set by the number of photons absorbed, and re-emitted, by the wind, which is fundamentally governed by the density profile as well as the incident X-ray spectrum originating from the central corona. Hence, the model takes as input parameters the normalisation and photon index of the incident spectrum. *These should always be tied to a corresponding fit of the broad-band continuum, and not left free while fitting the line-profile.* In addition to the self-consistent normalisation, xwindfe uses the 7-Lorentzian Hölzer et al. (1997) profile for the rest-frame emission. This leads to it naturally including Lorentzian wings, as well as both Fe-K α_1 and Fe-K α_2 lines. The input parameters for this model are given in tabel A.2.

xwindconv: Convolution model. Takes the line-profiles from xwindline, and uses them as a convolution kernel that is the applied to some input spectrum. Note that the normalisation used is such that the convolution conserves the photon number of the input spectrum (i.e if you convolve an input spectrum containing 100 photons with xwindconv the output spectrum will also contain 100 photons). The advantage here is that one can apply wind broadening to either continuum emission (e.g the diffuse continuum, under certain assumptions) or output line emission from e.g more realistic radiative transfer calculations (from e.g CLOUDY Ferland et al. 2017), again under the assumption that the emissivity follows the profile calculated here. The input parameters are given in table A.3.

Appendix B: Comparison to DISKLINE

As a sanity check we, we adapt our model to a Keplerian disc, allowing for a direct comparison to the well established DISKLINE (Fabian et al. 1989). The main differences from xwind are that we now only consider the Keplerian velocity component in Eqn. 15 (as well as the gravitational redshift). We also calculate the emission using a simple radial emissivity profile, with $\epsilon(r) \propto r^{-3}$.

The resulting line-profiles are shown in Fig. B.1, where we have performed comparisons while stepping through inner radius (left panel), and observer inclination (middle and right panels). DISKLINE is shown as the dashed black lines, while the profile from our code is shown as the solid coloured lines. For large radii, $r \gtrsim 50$, the profiles are entirely consistent with one another. This is not the case at small radii where we start to see

Parameter	Description	Units
$\log_{10} \dot{m}_w$	Wind mass outflow rate	$\dot{M}_w / \dot{M}_{\text{Edd}}$
r_{in}	Inner launch radius (see Fig. 1)	R_G
r_{out}	Outer launch radius	R_G
d_f	Distance from origin to wind focus (see Fig. 1)	R_G
f_{cov}	Wind covering fraction as seen from the central black hole	$\frac{\Omega}{4\pi}$
$\log_{10} v_{\infty}$	Outflow velocity at infinity (see Eqn. 6)	c
r_v	Velocity scale length. The distance along the streamline where the wind reaches half of v_{∞}	R_G
β	Wind velocity exponent. Determines the acceleration of the wind (see Eqn. 6)	Dimensionless
v_{turb}	Turbulent velocity. Assumed constant across the wind. Sets the width of the Gaussian smoothing kernel used to emulate turbulence.	km/s
κ	Sets the weighting for the wind launch efficiency as a function of radius. Larger values will weigh the mass-outflow towards larger radii (and vice-versa for lower values). See Eqn. 8	Dimensionless
Inc.	Observer inclination, measured from the z-axis	degrees
E0	Rest-frame energy of the emission line	keV
Norm.	Normalisation. Sets the total number of photons within the line	$\text{photons s}^{-1} \text{cm}^{-2}$

Table A.1: Parameters in xwindline. These are given in the order they should be passed to the code.

some systematic deviation. This is likely due to our choice of a flat-space time metric. While DISKLINE ignores light-bending, it does still calculate the energy shifts and impact parameters in the Schwarzschild metric. This becomes important at small radii. As such, we do not recommend the use of our model for very small launch radii (as might be expected from e.g. at UFO type wind).

Nonetheless, at BLR scales, the general relativistic corrections are negligible, with perhaps the exception of the gravitational redshift, which is included in our model.

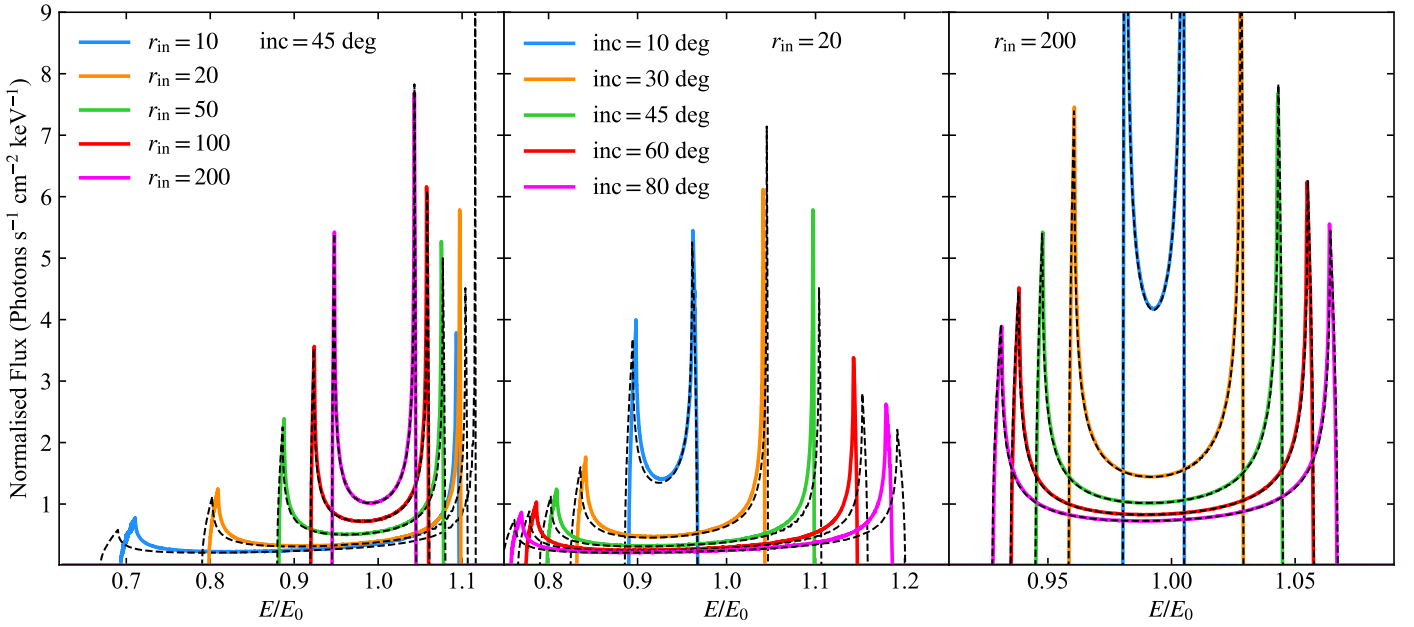


Fig. B.1: Comparison of line profiles for a Keplerian disc, calculated considering only relativistic Doppler shifts as outlined in section 2.5 (solid coloured lines) and calculated using the DISKLINE model (Fabian et al. 1989) (dashed lines), which includes some corrections expected from the Schwarzschild metric. In all cases these are calculated for a narrow annulus, such that $r_{\text{out}} = 1.1r_{\text{in}}$. The left panel shows the profiles while stepping through values of r_{in} , in order to highlight where our approximations break down. For $r_{\text{in}} \gtrsim 50$ our line profile matches that of DISKLINE well, whereas below this we start to see systematic offsets originating from our choice of metric. The middle and right panels show the profiles while stepping through observed inclination, with $r_{\text{in}} = 20$ and 200 respectively. Again, in the weak field limit, where general relativistic corrections are small, our approximation matches well that of DISKLINE.

Appendix C: Line-profile component tests

We present here a brief set of comparison fits to quantitate the significance of each component. In total we perform six additional fits, removing/including the xwindfe, mytorus, and DISKLINE components. The underlying continuum model is fixed to that presented in section 4. As with our fiducial model fit, we use the 5.0–6.6 keV range of the XRISM-resolve spectrum. The resulting fits are shown in Fig. C.1, with a zoom in on the residual shown in Fig. C.2. Each panel in the figures gives the relevant model combination to the line profile.

Perhaps the least significant component to the line profile is DISKLINE, with $\Delta\chi^2 = 75$ with only 2 additional degrees of freedom. This is not particularly surprising, given that broad components suffer from dilution with the underlying continuum, especially in high resolution spectra.

More importantly for this paper, we see both the MYTORUS and xwindfe components are significant, with $\Delta\chi^2 = 109$ and $\Delta\chi^2 = 145$ for 3 and 4 additional degrees of freedom respectively. It is quite clear in residuals shown in Fig. C.2 that these components are required to model the narrow and intermediary components to the line.

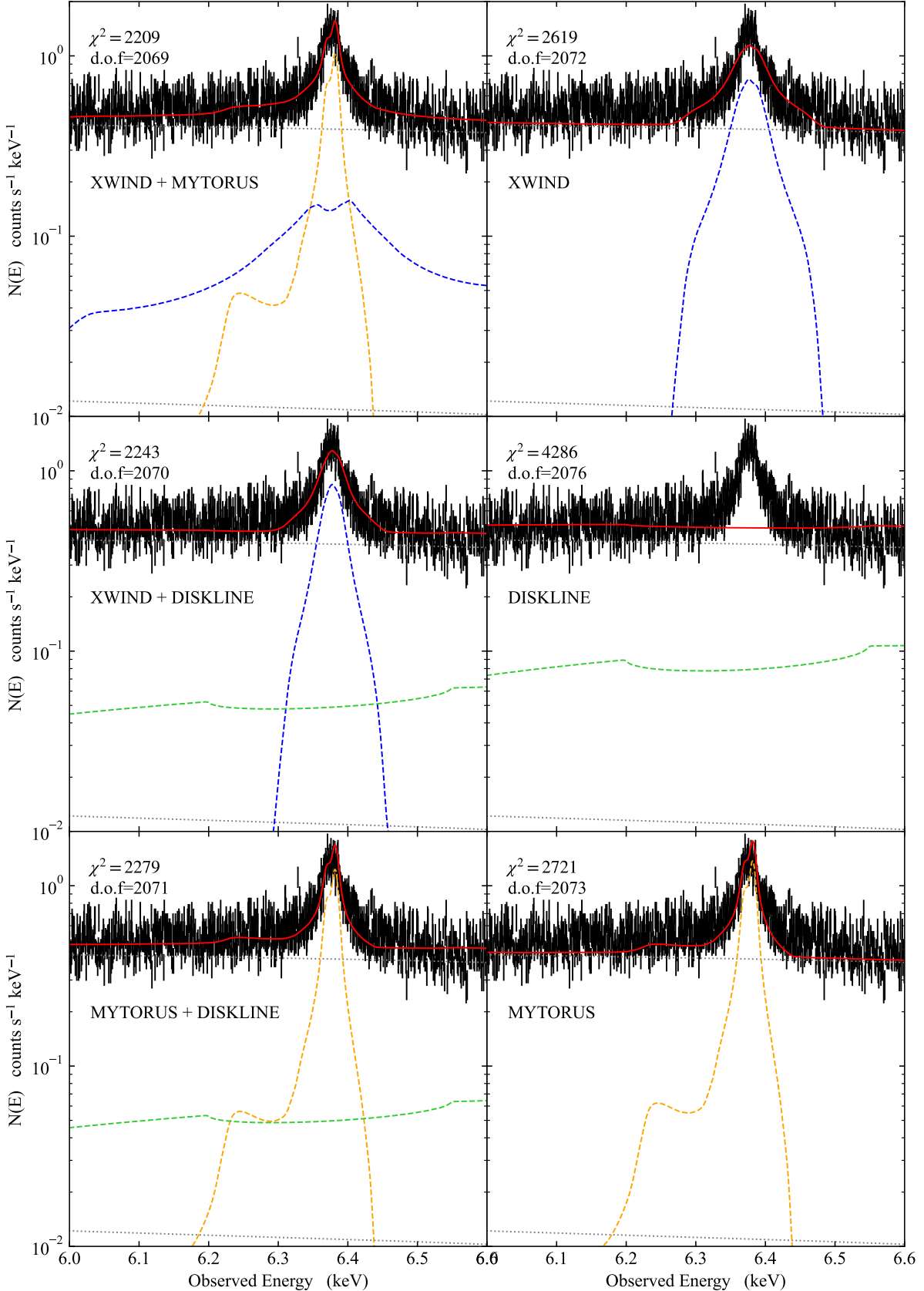


Fig. C.1: Model fits to XRISM-resolve for subsets of our total line-profile model, to highlight the significance of each component. As with the main model in Fig. 6 these have been fit over the 5.0–6.6 keV energy range. The left column shows the case for a two-component model to the Fe-K α complex, while the right shows a single component scenario. The relevant model components (shown as dashed coloured lines) are XWINDFE (blue), MYTORUS (orange), and DISKLINE (green). In all cases, these result in a statistically significantly worse fit than our fiducial three component model for the Fe-K α complex.

Parameter	Description	Units	Parameter	Description	Units
$\log_{10} \dot{m}_w$	Wind mass outflow rate	$\dot{M}_w / \dot{M}_{\text{Edd}}$	$\log_{10} \dot{m}_w$	Wind mass outflow rate	$\dot{M}_w / \dot{M}_{\text{Edd}}$
r_{in}	Inner launch radius (see Fig. 1)	R_G	r_{in}	Inner launch radius (see Fig. 1)	R_G
r_{out}	Outer launch radius	R_G	r_{out}	Outer launch radius	R_G
d_f	Distance from origin to wind focus (see Fig. 1)	R_G	d_f	Distance from origin to wind focus (see Fig. 1)	R_G
f_{cov}	Wind covering fraction as seen from the central black hole	$\frac{\Omega}{4\pi}$	f_{cov}	Wind covering fraction as seen from the central black hole	$\frac{\Omega}{4\pi}$
$\log_{10} v_{\infty}$	Outflow velocity at infinity (see Eqn. 6)	c	$\log_{10} v_{\infty}$	Outflow velocity at infinity (see Eqn. 6)	c
r_v	Velocity scale length. The distance along the streamline where the wind reaches half of v_{∞}	R_G	r_v	Velocity scale length. The distance along the streamline where the wind reaches half of v_{∞}	R_G
β	Wind velocity exponent. Determines the acceleration of the wind (see Eqn. 6)	Dimensionless	β	Wind velocity exponent. Determines the acceleration of the wind (see Eqn. 6)	Dimensionless
v_{turb}	Turbulent velocity. Assumed constant across the wind. Sets the width of the Gaussian smoothing kernel used to emulate turbulence.	km/s	v_{turb}	Turbulent velocity. Assumed constant across the wind. Sets the width of the Gaussian smoothing kernel used to emulate turbulence.	km/s
κ	Sets the weighting for the wind launch efficiency as a function of radius. Larger values will weigh the mass-outflow towards larger radii (and vice-versa for lower values). See Eqn. 8	Dimensionless	κ	Sets the weighting for the wind launch efficiency as a function of radius. Larger values will weigh the mass-outflow towards larger radii (and vice-versa for lower values). See Eqn. 8	Dimensionless
Inc.	Observer inclination, measured from the z-axis	degrees	Inc.	Observer inclination, measured from the z-axis	degrees
A_{Fe}	Iron abundance, relative to solar. Uses the abundance values from (Anders & Grevesse 1989)	$[\text{Fe}]/[\text{Fe}_{\odot}]$			Table A.3: Parameters in xwindconv.
N_0	Normalisation of the incident X-ray power-law emission	$\text{photons s}^{-1} \text{cm}^{-2}$ at 1 keV			
Γ	Photon index of the incident X-ray power-law spectrum	Dimensionless			

Table A.2: Parameters in xwindfe.

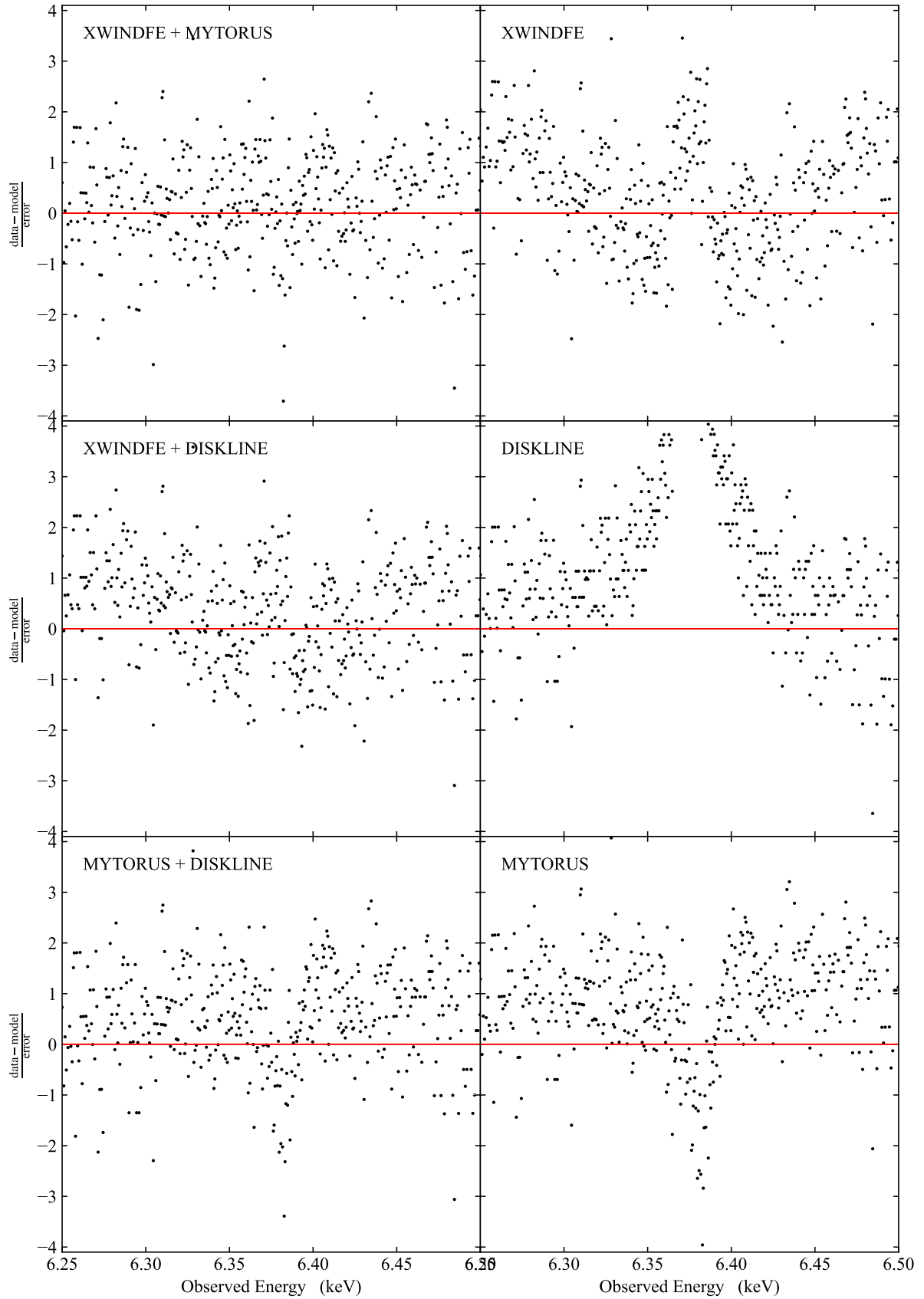


Fig. C.2: Residual to the fits presented in Fig. C.1. Note we have chosen to zoom in on the 6.25–6.5 keV region in order to highlight the residuals around the Fe- $\text{K}\alpha$ complex. The fits, however, are performed across the 5.0–6.6 keV range.